Acta Geologica Polonica, Vol. 70 (2020), No. 4, pp. 529–567
DOI: 10.24425/agp.2020.132262

Marine snow and epipelagic suspensoids in the Reda carbonates and a pronounced mid-Ludfordian (Silurian) CIE in the axis of the Baltic Basin (Poland)

WOJCIECH KOZŁOWSKI

Faculty of Geology, University of Warsaw,
Żwirki i Wigury 93, PL-02-089 Warsaw, Poland. E-mail: woko@uw.edu.pl

ABSTRACT:

Kozłowski, W. 2020. Marine snow and epipelagic suspensoids in the Reda carbonates and a pronounced mid-Ludfordian (Silurian) CIE in the axis of the Baltic Basin (Poland). *Acta Geologica Polonica*, **70** (4), 529–567. Warszawa.

The mid-Ludfordian pronounced, positive carbon isotope excursion (CIE), coincident with the Lau/kozlowskii extinction event, has been widely studied so far in shallow-water, carbonate successions, whereas its deep-water record remains insufficiently known. The aim of this research is to reconstruct the sedimentary environments and the palaeoredox conditions in the axial part of the Baltic-Podolian Basin during the event. For these purposes, the Pasłęk IG-1 core section has been examined using microfacies analysis, framboid pyrite diameter and carbon isotope measurements. The prelude to the event records an increased influx of detrital dolomite interpreted as eolian dust, coupled with a pronounced decrease in the diameter of the pyrite framboids, indicating persistent euxinic conditions across the event. The event climax is recorded as the Reda Member and consists of calcisiltites, composed of calcite microcrystals ('sparoids'), which are interpreted as suspensoids induced by phytoplankton blooms in the hipersaturation conditions present in the epipelagic layer of the basin. Both the prelude and climax facies show lamination, interpreted as having resulted from periodical settling of marine snow, combined with hydraulic sorting within a 'benthic flocculent layer', which additionally may be responsible for a low organic matter preservation rate due to methanogenic decomposition. Contrary to the observed basinward CIE decline in the benthic carbonates in the basin, the Reda Member records an extremely positive CIE (up to 8.25‰). Given the pelagic origin of the sparoids, the CIE seems to record surface-water carbon isotope ratios. This points to a large carbon isotope gradient and kinetic fractionation between surface and bottom waters during the mid-Ludfordian event in a strongly stratified basin. The Reda facies-isotope anomaly is regarded as undoubtedly globally triggered, but amplified by the stratified and euxinic conditions in the partly isolated, Baltic-Podolian basin. Hence, the common interpretation of the basin record as representative for the global ocean needs to be treated with great caution.

Key words: Pelagic carbonates; Sparoids; Marine snow; Algal blooms; Eolian dust; Carbonate supersaturation; Euxinia; Baltic Basin; Reda Member, Ludlow; Silurian.

INTRODUCTION

The mid-Ludfordian contains a globally recorded, facies-geochemical event, coinciding with the Lau conodont (Jeppsson and Aldridge 2000) and *kozlowskii* graptolite (Koren 1993, Urbanek 1993) extinctions (summarized in Calner 2008; Jeppsson *et al.* 2012; Munnecke *et al.* 2010). One of the most conspicuous features of this event is the pronounced positive mid-Ludfordian carbon isotope excursion (CIE),

globally recorded in the carbonate successions of low and middle palaeolatitudes (e.g. Frýda and Manda 2013; Jeppsson *et al.* 2012; Spiridonov *et al.* 2017; Younes *et al.* 2017 and references therein). The sedimentary record of the event closely resembles other CIE-related early Palaeozoic perturbations (summarized in fig. 6 in Munnecke *et al.* 2003), which probably represent the repercussions of short-lived glaciations in low-palaeolatitudes (see discussion in Cherns and Wheeley 2009; Kaljo *et al.* 1996; Kaljo *et al.* 2003). According to Munnecke *et al.* (2003), typical sedimentary features of these CIE-related events observed in shallow-water tropical shelf successions include: (1) proliferation of carbonate platforms, particularly through the intensification of microbial-biochemical and (quasi-) chemogenic carbonate precipitation; (2) a sequence boundary near the base of the event; (3) abundant terrigenous silt admixture, often interpreted as being of eolian origin (e.g. Kozłowski and Sobień 2012; Samtleben *et al.* 2000); (4) coincident low diversity of plankton communities and minor extinctions; and (5) short duration (low relative thickness). Munnecke *et al.* (2003) have noticed also that the events are not coeval with the deposition of anoxic sediments *sensu* organic matter (OM) accumulations in deep shelf environments, which, in turn, is observed below and above the event interval. Loydell (2007) complemented the list by basinward decline of the CIE amplitude; however, CIEs with a minor amplitude are recorded in organic matter (OM) carriers also in deep shelf (Noble *et al.* 2012) and oceanic settings (Melchin and Holmden 2006a; Underwood *et al.* 1997). The maximum amplitude of CIEs, especially during the mid-Ludfordian CIE, which is extreme in amplitude (up to +12), seems to be locally amplified by isotope fractionations in carbonate-bearing epeiric seas with limited circulation (Holmden *et al.* 2012; Kozłowski 2015; Kozłowski and Sobień 2012). Despite a similar scenario of the early Palaeozoic events and a general consensus on their glacial trigger, the nature and origin of CIEs is still the subject of debate (summarized and discussed in Calner 2008; Ghienne *et al.* 2014; Kozłowski 2015; Loydell 2007; Melchin and Holmden 2006a; Munnecke *et al.* 2010; Munnecke *et al.* 2003; Noble *et al.* 2012).

The late Silurian, Caledonian (Tornquist branch) foreland of the East European Craton, extending from Scania in Sweden to Podolia in the Ukraine (Central Europe; Text-fig. 1), is one of the type areas of the Lau/*kozlowskii* event, intensively studied in recent years (Eriksson and Calner 2008; Jeppsson *et al.* 2012; Jeppsson *et al.* 2007; Kaljo *et al.* 2015; Kaljo *et al.* 2007; Kozłowski 2015; Kozłowski and Munnecke 2010; Kozłowski and Sobień 2012; Martma *et al.* 2010; Spiridonov *et al.* 2017; Younes *et al.* 2017). The record of the Lau/*kozlowskii* event in the Baltic-Podolian Basin is well recognised in its littoral part with an extended carbonate platform. In the most proximal parts, sea-level fall caused a hiatus due to emersion (Eriksson and Calner 2008; Kaljo *et al.* 2015; Kaljo *et al.* 1997; Kozłowski and Munnecke 2010), whereas facies shift resulted in extensive carbonate (e.g. Martma *et al.* 2010) and/or clastic-carbonate (Eriksson and Calner 2008; Kozłowski and Munnecke 2010) shallow-water sedimentation in a more distal ramp setting (Text-fig. 1).

The record of the event in deep-water settings of the basin is poorly recognized. In the offshore palaeobasin in the subsurface area of Poland, the event interval is marked by a distinct negative, natural gamma-ray anomaly (Topulos 1976; Topulos 1977), used by Tomczyk (e.g. 1970) for tracking the 'middle Siedlce' horizon, referred to the *Neocucullograptus–Formosograptus* graptolite interregnum (with the base coeval with the *kozlowskii* event of (Urbanek 1993). Kozłowski and Sobień (2012) have shown that the 'middle Siedlce' geophysical marker in a periplatform setting (Mielnik IG-1 borehole section, no. 14 in Text-fig. 1), corresponds to a distinct facies anomaly, coeval with the mid-Ludfordian CIE. The anomaly is expressed by a mass admixture of calcite, dolomite and quartz silt forming a peculiar limestone-marl horizon, referred in northern Poland to the Reda Member (Modliński *et al.* 2006; Porębski and Podhalańska 2019).

The Reda Member in the periplatform setting of the Mielnik IG-1 borehole section contains abundant detrital silt (quartz, dolomite), which was interpreted as eolian-derived (Kozłowski 2015; Kozłowski and Sobień 2012). The mass appearance of minute euhedral calcite crystals was taken as massive carbonate precipitation in the water-column (whitings) caused by carbonate hypersaturation conditions (Kozłowski 2015). The anomalous facies in the Mielnik IG-1 borehole section records a moderate-high CIE amplitude in bulk rock samples (+6.74‰), resulting from the mixing of epipelagic calcite with $\delta^{13}C$ values ~10‰, suppressed by admixture of eolian dolomite with low (~0‰) $\delta^{13}C$ values (Kozłowski 2015). Despite the lack of OM accumulation, synchronous pronounced changes in the diameter of pyrite framboids in the carbonate horizon indicate the development of euxinic conditions in the water column (Kozłowski 2015), which was confirmed later by geochemical proxies from other parts of the basin (Bowman *et al.* 2019).

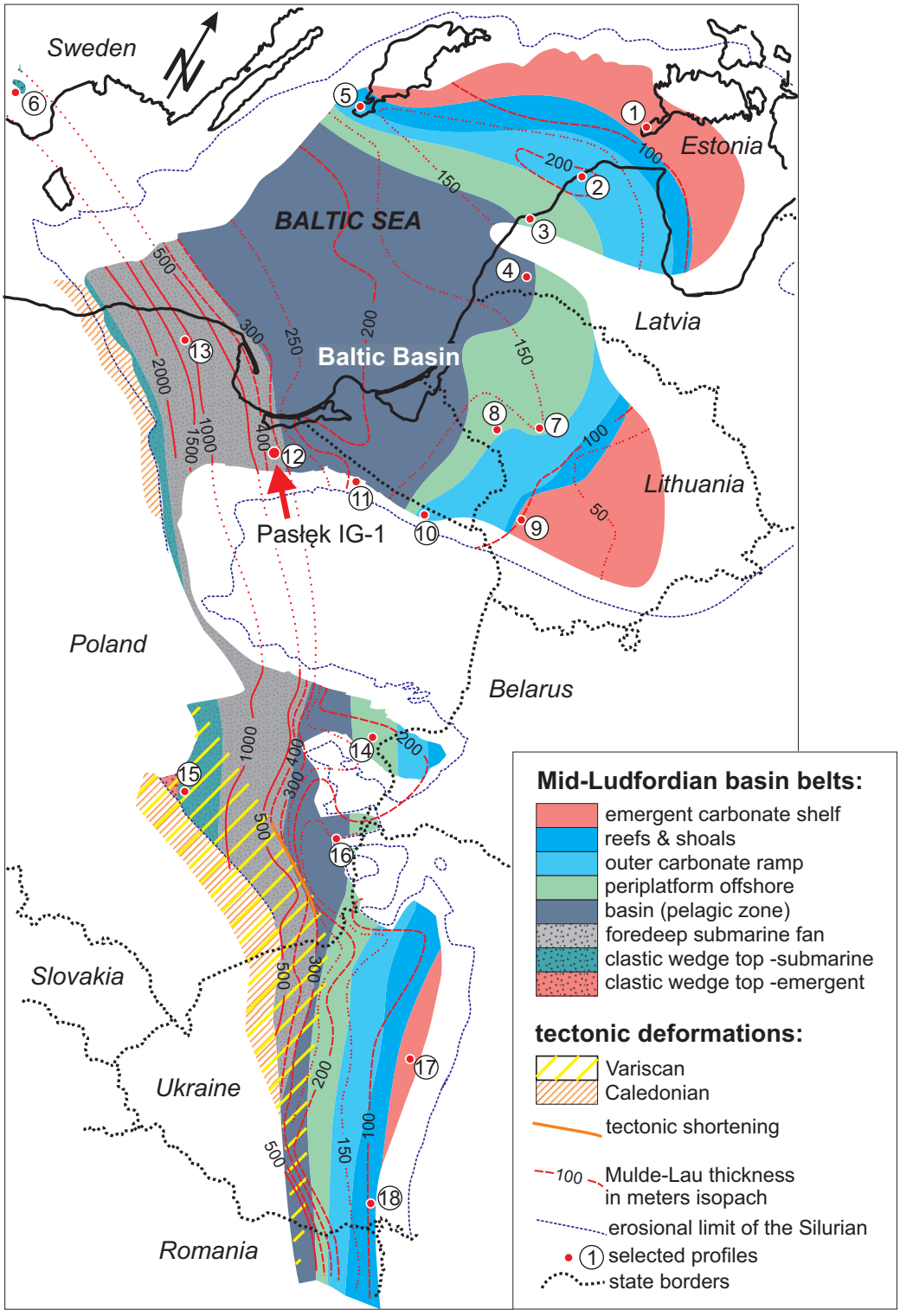

Text-fig. 1. Location of the Pasłęk IG-1 borehole section (arrowed) against Silurian palaeogeography and facies distribution (based on Bassett *et al.* 1989) during the mid-Ludfordian regression on the SW margin of the East European Craton. The isopachs (red lines) illustrate the thickness of the rocks occurring between the mid-Homerian (Mulde) and mid-Ludfordian (Lau) reference geophysical anomalies. Selected Silurian sections: 1 – Ohessaare-1; 2 – Ventspils-D3; 3 – Pavilosta-1; 4 – Priekule-1; 5 – Gotland; 6 – Skåne; 7 – Vidukle-61; 8 – Milaičiai-103; 9 – Vilkaviškis-134; 10 – Gołdap IG-1; 11 – Bartoszyce IG-1; 12 – Pasłęk IG-1; 13 – Lębork IG-1; 14 – Mielnik IG-1; 15 – Rzepin (Holy Cross Mts.); 16 – Syczyn OU-1; 17 – Kotiuzhyny-1; 18 – Zvanets (Podolia).

The Reda Member gamma-ray anomaly seems to be palaeobathymetrically independent and may be tracked basinward, to the clay-dominated, basinal facies zone (Kozłowski and Sobień 2012; Porębski and Podhalańska 2019; Porębski *et al.* 2013; Topulos 1977). These observations suggest the pan-basinal extent of the massive epipelagic calcite precipitation and eolian dolomite admixture, extending also in the distal and strictly pelagic realm.

Based on this statement, the aim of this study is to investigate the facies-geochemical record of the Reda anomaly (Lau/*kozlowskii* event) in the maximally offshore – deep water part of the Baltic Basin, particularly in terms of: (I) comparing the facies development between the periplatform (Mielnik IG-1 borehole section) and strictly pelagic settings; (II) reconstructing the sedimentary conditions and processes leading to the formation of unusual pelagic carbonates; (III) understanding the time relation between the facies anomaly and the development of euxinic conditions in the deepest part of the basin; and (IV) determining the amplitude of the carbon isotope excursion in context of its lateral and paleobathymetric variation. For these aims, the Reda Member succession from the basin axis, represented by the Pasłęk IG-1 borehole section in northern Poland (Text-fig. 1), has been studied in terms of sedimentology (microfacies), the carbon and oxygen stable isotope record and the record of redox conditions based on the distribution of pyrite framboid diameters.

GEOLOGICAL AND PALAEOGEOGRAPHIC SETTING

The Ediacaran to lower Palaeozoic succession of NE Poland forms the lower part of the sedimentary cover of the East European Craton, which comprised the Baltica sector of the Laurussia palaeocontinent in the middle Palaeozoic. During the late Silurian, the area was located in the tropics (Cocks and Torsvik 2005), which resulted in the presence of the carbonate-bearing successions of palaeolittoral areas. The belt of shallow-water carbonate platforms can be traced from Gotland island (Sweden) in the north, to Besarabia (Romania and Moldova) in the south (Text-fig. 1). The more distal part of the craton margin, extending from NW to SE across central Poland, evolved during the Silurian from an epicratonic marginal shelf basin into the foreland basin of the southern branch of the Caledonian orogen (Poprawa *et al.* 1999), as a consequence of oblique arc-continent collision with the Teisseyre Arc (see e.g. Kozłowski *et al.* 2014).

During the Ludlow, massive clastic influx from the newly formed Tornquist branch of the Caledonian orogen overfilled the proximal (SW) part of the foredeep (Jaworowski 1971), creating a novel littoral zone (n. 15 in Text-fig. 1; Kozłowski 2003) located opposite the main (Gotland-Estonia-Podolian) carbonate shelf. As a result of such palaeogeographic changes, the earlier open shelf basin was transformed into elongated epicratonic seaway. Because the Baltic Basin is the only northernmost, erosive remnant of such a paleobasin (see Text-fig. 1), it is proposed here to name it as the Baltic-Podolian (or Paratornquist analogously as Paratethys) Sea (or Basin).

It is important to note that the continuous occurrence of an open marine fauna across the Lau event in the basin (e.g. Martma *et al.* 2010; Spiridonov *et al.* 2017; Urbanek 1997) indicates persistent normal-marine conditions during the mid-Ludfordian lowstand, despite palaeogeographical restrictions. The most probable connection with the ocean could have been located in the far south-east, where still existent plate divergence is recorded by the numerous pyroclastic beds in the Ludlow-Přídolí succession of Podolia (Huff *et al.* 2000).

The studied section of the Pasłęk IG-1 deep borehole (Text-fig. 2A) is located in the Peribaltic Syneclise (southern Baltic Basin) in northern Poland (n. 12 in Text-fig. 1, arrowed). The section was selected for this study following a palaeogeographic, facies and thickness pattern analysis. The pattern of changes in thickness between the Mulde and Lau event-associated natural negative gamma anomalies (isopach in Text-fig. 1), indicates that the studied section represents the most distal part of the foredeep clastic wedge, hence it is representative for the basin axis facies zone. The event-related carbonate marker of the Reda Member occurs within the Kociewie Formation (Text-fig. 2A), recognised as comprising flysch-like sedimentary rocks, deposited with the participation of turbidity currents (Jaworowski 1971; Jaworowski 2000) in a distal foredeep setting. Subsequent elements of the Silurian succession of the Pasłęk IG-1 borehole section (Tomczyk 1973) are in general typical for the entire SW margin of the East European Craton.

The stratigraphically incomplete Llandovery succession (see Text-fig. 2A) is represented by an only 20 m thick complex of black siliceous shales (Pasłęk Formation), succeeded by 230 m of dark-grey clayey graptolitic shales (Pelplin Formation) representing the Wenlock and lower Ludlow. The general lack of benthic fauna, abundant graptolites and scarcity of primary carbonates are consistent with its pelagic sedimentary setting and basinal palaeogeographic

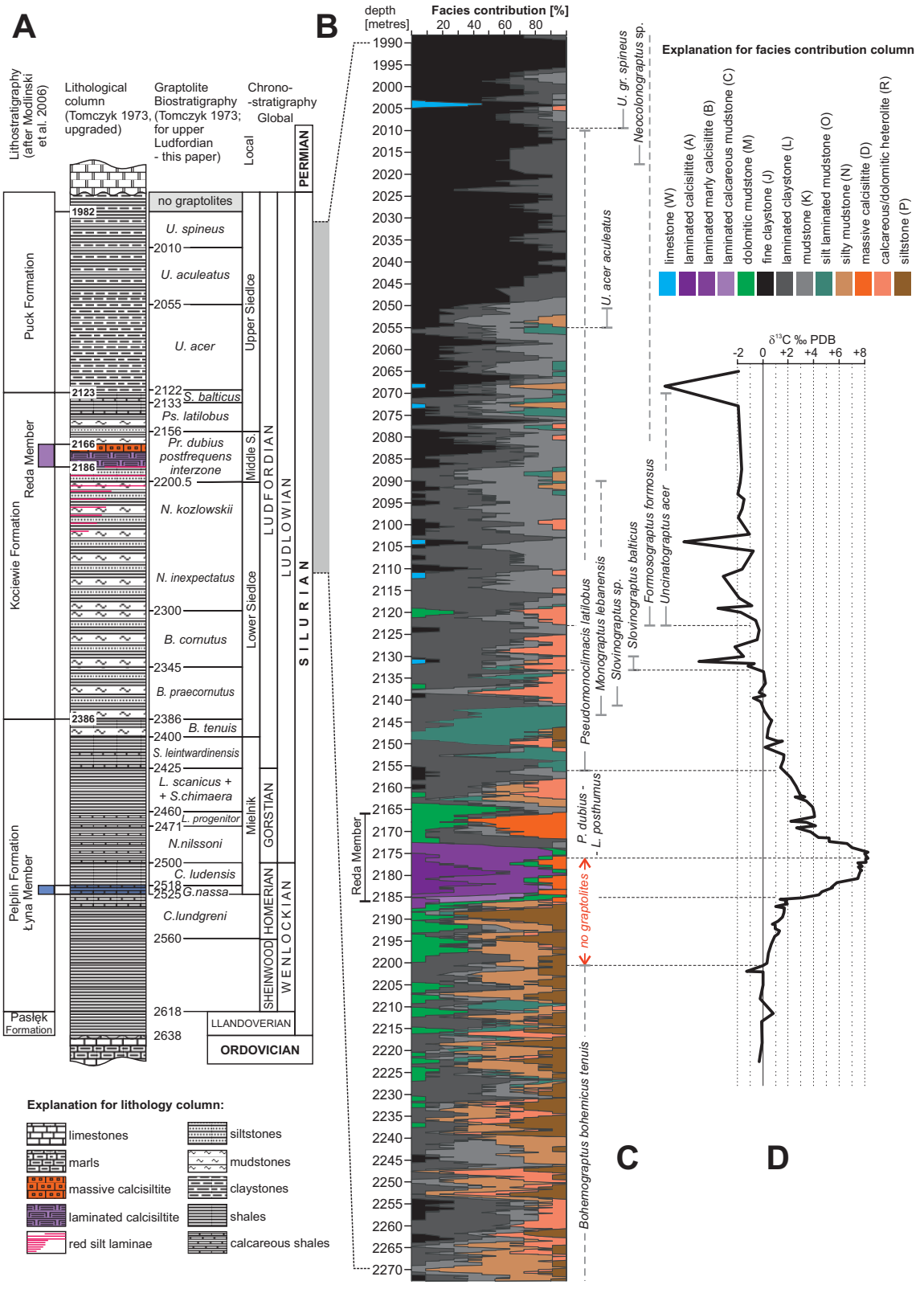

Text-fig. 2. A – Vertical column (scaled to depth) of Silurian strata in the Pasłęk IG-1 borehole; B – Detailed vertical changes in the facies contribution of the upper Ludfordian in the Pasłęk IG-1 borehole; C – Graptolite ranges in the section; D – General bulk carbonate carbon isotope curve (this paper).

position. The main pronounced facies anomaly within this interval occurs at the top of the *Cyrtograptus lundgreni* Zone (2525 m, Text-fig. 2A) with the appearance of a rich non-graptolitic fauna, carbonate admixture and pronounced, natural gamma-ray low. The anomaly, coeval with the Mulde/lundgreni event (Porębska *et al.* 2004) in the neighbouring Prabuty IG-1 and Olsztyn IG-2 borehole sections (incomplete core interval in the Pasłęk IG-1 borehole), was recognised (Zenkner and Kozłowski 2017) as an older facies analogue of the Reda Member (named Łyna Member; Text-fig. 2A).

The lower Silurian graptolitic shales are followed (above the *Saetograptus leintwardinensis* Zone – Tomczyk 1973) by the flysch-like Kociewie Formation, early to middle Ludfordian in age. The formation in the Pasłęk IG-1 borehole section is dominated by the presence of fine-grained components of the Bouma sequence (F3–F4 facies of Jaworowski 2000), and it is interpreted as being deposited in a deep-water plain, influenced by distal turbidites in a foreland setting (Poprawa *et al.* 1999). The relatively lowest (in observed range) thickness for the Kociewie Formation in the Pasłęk IG-1 borehole section (270 m) points to the basin-axis position of the profile in the general palaeobathymetric and subsidence pattern (Text-fig. 1).

The uppermost part of the Kociewie Formation in the Pasłęk IG-1 borehole section is interrupted by the relatively thin (20 m) carbonate-bearing Reda Member, consisting of laminated marlstones and calcisiltites (Modliński *et al.* 2006; Text-fig. 2A). Originally, Tomczyk (1970) referred this interval to the "Middle Siedlce Beds", defined by him in Poland as beds containing a low-diversity pristiograptid graptolite fauna, occurring above the last appearance of the *Bohemograptus–Neocucullograptus* assemblage (*kozlowskii* extinction event of Urbanek 1993) and below the flourishing of the *Formosograptus* graptolite fauna assemblages.

The Reda Member is succeeded by the topmost part of the Kociewie Formation and the clay dominated Puck Formation, containing an upper Ludfordian graptolite assemblage. Post-Silurian and pre-Permian erosion resulted in the lack of Přídolí deposits in the studied section. The basinal facies of the Přídolí occur further northwards towards the Baltic Sea area, where development of an open marine basin is documented up to the Silurian–Devonian boundary.

MATERIAL AND METHODS

Almost 100% of the Pasłęk IG-1 borehole was cored (see Text-fig. 3B). The archival material in the studied interval is almost complete. Section measuring was performed in the drill core storage. The macrofacies determination was carried out by comparison with a reference sample palette, prepared from samples representative for the macrofacies spectrum observed during a preliminary core overview. The macrofacies were determined in constant span points, with a resolution of 0.1 m (0.05 m in the Reda Member interval). The codified macrofacies record was subsequently processed in Excel software and exported as graphic logs (Text-fig. 3A, B). Graptolites observed during the analysis were photographed and used for updating of the existing archival biostratigraphic data (Tomczyk 1973; Text-figs 2A, C; 3A).

Microfacies analysis was performed on a set of 90 uncovered, finely polished, and additionally thinned (10–20 μm) thin sections, stained (etched) in Dickson's solution. The solution produces a pink to red stain on the calcite surface, with saturation and hue depending on crystal size, orientation and presence of chemical impurities (especially iron admixture). The dolomite remains unstained. The observations were performed in transmitted, as well as combined 40% transmitted and 60% reflected light in NikonEclipse LV100POL with 2×-60× Plan Fluor lens and LUCIA software with parallel examination of thin sections and raw rock fragments in an SEM-backscatter with EDS in the Microanalysis Laboratory of the Faculty of Geology, University of Warsaw. The semi-quantitative mineral composition of 58 bulk rock samples across the studied interval was determined using XRD analysis (standard Bragg-Brentano method) in the XRD Laboratory of the Faculty of Geology, University of Warsaw.

Text-fig. 3. Detailed logs of the mid-Ludfordian CIE interval in the Pasłęk IG-1 borehole section: A – graptolite ranges; B – lithological log; → scales: depth in metres; succeeding core intervals with archival box numbers (from-to); rectangles – archival boxes, red colour – lack of core; C – bulk carbonate carbon isotope data, colours of circles indicate facies affiliation of the analysed sample; D – bulk carbonate oxygen isotope data recalculated according to Rosenbaum and Sheppard (1986) for dolomite admixture (using semi-quantitative XRD data); E – box-and-whisker plots of pyrite framboid sizes, 5 and 10 μm size limits marked by black vertical lines; red solid lines showing the pyrite content [‰]; F – natural gamma log; G – magnetic susceptibility log; H – vertical changes in the mineralogical composition (semi quantitative XRD data) of the samples subdivided into "pelagic" (left scale) and "detrital" (right scale) components, dotted black line shows vertical changes in the contribution of dolomite in the terrigenous silt [dolomite/(dol + Q + F ratio)].

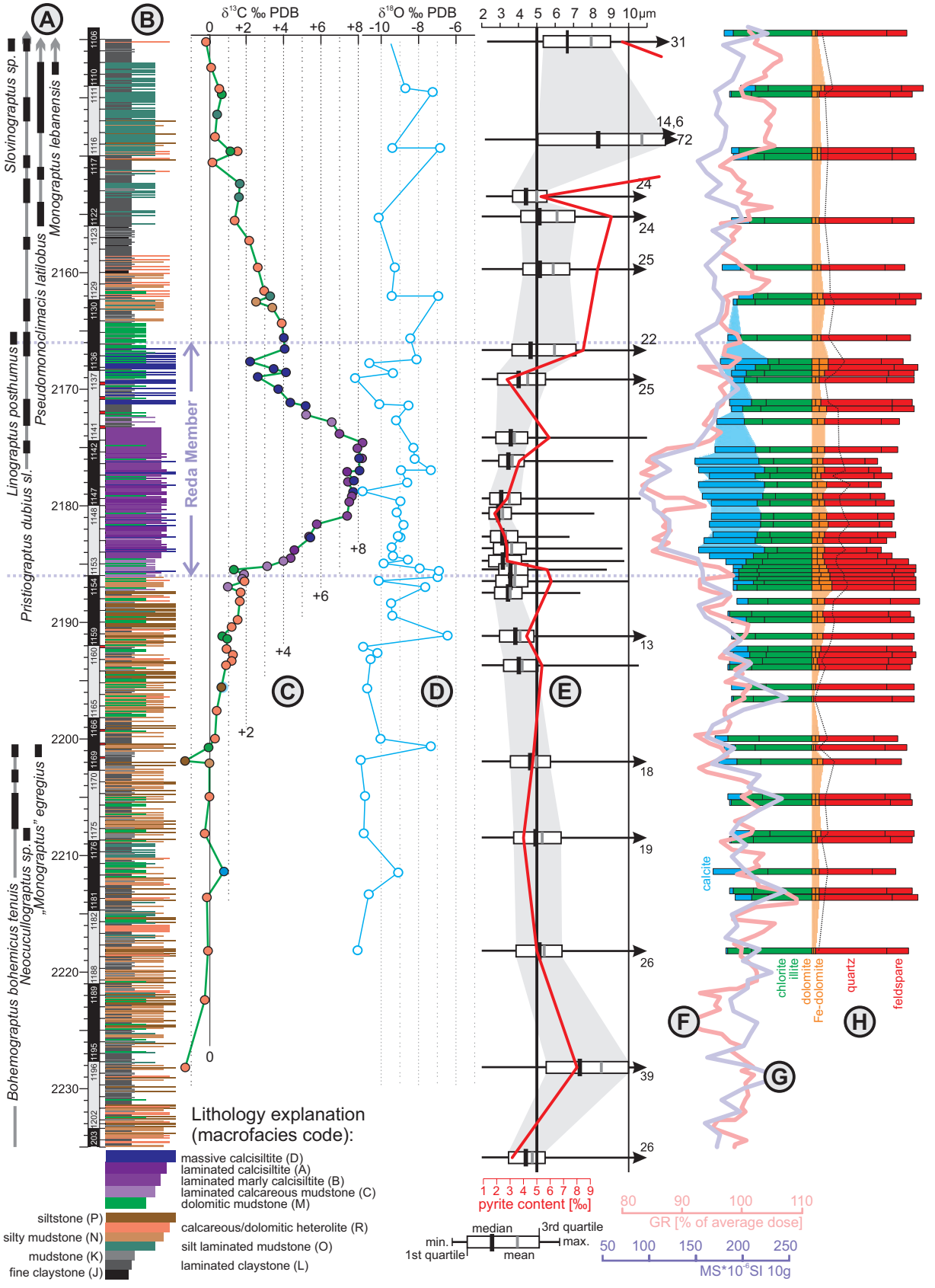
A
B
C
D
E
F
G
H
Slovinograptus sp.
Monograptus lebanensis
Pseudomonoclimacis latilobus
Linograptus posthumus
Pristiograptus dubius sl.
Reda Member
Bohemograptus bohemicus tenuis
Neocucullograptus sp.
„Monograptus" egregius
δ13C ‰ PDB
δ18O ‰ PDB
2160
2170
2180
2190
2200
2210
2220
2230
pyrite content [‰]
median
3rd quartile
min.
max.
1st quartile
mean
GR [% of average dose]
MS*10-6SI 10g
calcite
chlorite
illite
dolomite
Fe-dolomite
quartz
feldspare
Lithology explanation
(macrofacies code):
massive calcisiltite (D)
laminated calcisiltite (A)
laminated marly calcisiltite (B)
laminated calcareous mudstone (C)
dolomitic mudstone (M)
siltstone (P)
silty mudstone (N)
mudstone (K)
fine claystone (J)
calcareous/dolomitic heterolite (R)
silt laminated mudstone (O)
laminated claystone (L)

	sample	depth	examined area (sq. mm)	N	pyrite content [%]	pyrite framboids diameter min	max	mean	1Q	median (2Q)	3Q	SD	skew-ness	grains under 5μm [%]	pyrite type	interpreted paleoredox conditions	
	Ps1107g	2140.3	1.28	294	1.14	2.29	31.45	7.96	5.35	6.66	9.01	4.28	1.99	21	D	upper dysoxic	
	Ps1115s	2148.5	1.00	340	3.08	2.17	71.99	10.72	5.06	8.34	14.60	8.19	2.67	25	D	upper dysoxic	
	Ps1120d	2153.7	1.14	309	0.53	2.23	24.12	5.00	3.68	4.41	5.55	2.29	3.47	67	B	lower dysoxic	
	Ps1122d	2155.4	0.85	311	1.06	1.77	23.99	6.10	4.13	5.14	7.07	3.32	2.18	45	C	middle dysoxic	
	Ps1126d	2159.7	0.85	301	0.96	1.68	25.44	5.89	4.24	5.16	6.79	2.95	2.52	48	C	middle dysoxic	
Reda member	Ps1135s	2167.6	1.00	303	0.85	1.67	21.70	5.96	3.65	4.66	7.13	3.82	1.89	58	C	middle dysoxic	laminated calcisiltites
	Ps1137s	2168.9	1.85	326	0.28	1.45	25.15	4.50	2.86	4.01	5.47	2.46	2.98	71	B	lower dysoxic	
	Ps1141d	2174.2	0.57	301	0.59	1.45	12.36	3.78	2.77	3.58	4.50	1.36	1.33	82	A2	temporary euxinic	
	Ps1143d	2176.1	0.85	302	0.37	1.79	9.16	3.66	2.93	3.45	4.31	1.09	1.08	89	A1	euxinic	
	Ps1146s up	2178.4	0.71	333	0.56	1.46	12.08	3.90	2.81	3.54	4.63	1.57	1.49	81	A2	temporary eux.	
	Ps1146s low	2178.4	3.27	345	0.35	1.53	20.12	6.48	3.74	5.48	7.92	3.46	1.19	45	C	middle dysoxic	
	Ps1146d	2178.9	1.14	327	0.28	1.29	11.21	3.50	2.44	3.06	4.13	1.60	1.76	85	A1	euxinic	
	Ps1148d	2180.7	1.28	305	0.18	1.26	8.13	3.14	2.40	2.90	3.61	1.12	1.40	93	A1	euxinic	
	Ps1150d	2182.7	1.00	303	0.26	1.41	6.78	3.30	2.48	3.12	3.96	1.05	0.72	92	A1	euxinic	
	Ps1151d	2183.7	1.14	302	0.27	1.47	9.66	3.63	2.64	3.33	4.42	1.33	1.14	83	A1	euxinic	
	Ps1152d	2184.7	1.14	350	0.28	1.36	9.76	3.39	2.40	3.15	4.16	1.32	1.07	89	A1	euxinic	
	Ps1153d	2185.7	0.71	356	0.58	1.47	8.81	3.83	2.93	3.57	4.51	1.24	0.90	83	A1	euxinic	
	Ps1154_20	2186.2	0.57	305	0.61	1.57	9.97	3.79	2.77	3.56	4.51	1.32	1.33	83	A1	euxinic	
	Ps1155_60	2187.6	0.57	326	0.57	1.47	7.37	3.55	2.70	3.43	4.19	1.17	0.84	89	A1	euxinic	
	Ps1159_20	2191.2	1.00	323	0.42	1.41	13.25	4.08	2.97	3.83	4.84	1.50	1.50	77	A2	temporary euxinic	
	Ps1161m	2193.5	1.00	390	0.54	1.36	11.03	4.20	3.19	4.02	5.06	1.43	0.99	73	A2	temporary euxinic	
	Ps1169_15	2201.9	1.28	309	0.47	1.76	18.43	4.97	3.56	4.64	5.74	2.04	1.89	60	B	lower dysoxic	
	Ps1175_80	2208.5	1.71	311	0.40	1.72	19.28	5.29	3.74	4.93	6.32	2.25	2.24	51	B	lower dysoxic	
	Ps1185_20	2217.9	1.42	314	0.50	1.96	26.49	5.40	3.87	5.14	6.37	2.31	3.35	46	B	lower dysoxic	
	Ps1196g	2227.9	2.28	320	0.80	1.91	39.83	8.51	5.51	7.34	9.99	4.96	1.98	22	D	upper dysoxic	
	Ps1205s	2235.9	1.71	306	0.32	1.34	26.35	4.75	3.46	4.40	5.45	2.30	3.87	65	B	lower dysoxic	

Table 1. Size statistics of pyrite framboids in the mid-Ludfordian Reda Member and adjacent deposits of the Pasłęk IG-1 borehole section, with interpretation of the palaeoredox conditions.

Statistical counting and measurement of pyrite framboids were performed on the scaled SEM-backscatter images of thin sections using LUCIA software, with a precision greater than 0.1 μm. The measurements and counting were performed only for well-preserved, well-shaped and non-aggregate framboids. Euhedral, shapeless or aggregated pyrites (all categories rarely observed), were rejected from the measurement procedure. The diameters of framboidal pyrites were measured along serial parallel scanning sectors (150 μm width), perpendicular to lamination, across each thin-section until a size population of more than 300 framboids was achieved, or to the end of the measurement sector (resulting in >300 populations). The measured apparent diameters of pyrite framboids are smaller than the true values, but the deviation is less than 10% (Wilkin *et al.* 1996; Wignall and Newton 1998). The minimal, mean and maximum diameter; the standard deviation of diameters, the percentage of pyrite framboids with diameter ≥10 μm and pyrite content [‰] in samples were calculated from the measured framboidal pyrite population in each sample and the known size of the investigated area. The analytical results are listed in Table 1. The data have been presented (Text-fig. 3E) in the form of standard box and whisker plots proposed by Wignall and Newton (1998).

$\delta^{13}C$ and $\delta^{18}O$ values were measured in 107 bulk rock samples in the Stable Isotope Laboratory of the Polish Academy of Sciences in Warsaw. Each powdered sample was treated with 104% orthophosphoric acid at 70°C in a Thermo Kiel IV preparation system and analysed in a conjunct Thermo-Finnigan Delta Plus mass spectrometer in a Dual Inlet system. The values are reported in the conventional delta notation in per mil with respect to the Vienna Pee Dee Belemnite

sample	depth	facies	$\delta^{13}C$	calcite/ /dolomite	$\delta^{18}O$ corrected	$\delta^{18}O$ sample	
Ps1033w	2068.3	W	-7.70			*-6.95*	
Ps1039w	2072.9	W	-1.96			*-6.06*	
Ps1053s	2087.3	R	-1.68			*-9.48*	
Ps1056s	2090.3	R	-1.80			*-9.58*	
Ps1059g	2093.0	R	-2.00			*-10.14*	
Ps1060g	2094.1	R	-1.51			*-9.18*	
Ps1062s	2096.3	R	-1.65			*-9.43*	
Ps1064s	2098.3	R	-1.95			*-10.25*	
Ps1068g	2102.1	R	-1.09			*-8.99*	
Ps1070gw	2103.9	W	-6.23			*-4.82*	
Ps1072	2105.9	O	-0.75			*-8.76*	
Ps1076g	2110.1	R	-1.66			*-9.88*	
Ps1078g	2111.7	W	-3.14			*-6.26*	
Ps1082d	2116.7	R	-1.88			*-10.21*	
Ps1083_95	2118.4	O	-0.87			*-9.82*	
Ps1084s	2119.0	R	-3.54			*-7.92*	
Ps1085s	2120.0	R	-1.75			*-10.62*	
Ps1087g	2121.8	R	-0.58			*-9.39*	
Ps1089s	2124.0	R	-0.31			*-9.31*	
Ps1091d	2126.2	R	-0.47			*-9.02*	
Ps1093g	2127.8	O	-2.21			*-6.63*	
Ps1095s	2130.0	R	-1.52			*-8.50*	
Ps1096w	2131.2	W	-5.06			*-4.33*	
Ps1097_05	2131.6	P	-0.69			*-9.69*	
Ps1097d	2132.2	R	-1.18			*-10.45*	
Ps1099g	2133.5	R	0.05			*-9.41*	
Ps1102s	2136.2	R	0.20			*-9.19*	
Ps1104s	2138.2	R	-0.31			*-9.37*	
Ps1105_20	2138.9	R	0.14	63/37	-9.64	*-9.03*	
Ps1106s	2139.5	R	-0.78			*-9.35*	
Ps1107g	2140.3	R	-0.18			*-9.27*	
Ps1109s	2142.5	R	0.11			*-9.23*	
Ps1111g	2144.3	R	0.55	53/47	-8.68	*-7.92*	
Ps1111_65	2144.6	M	0.68	20/80	-7.25	*-5.95*	
Ps1113s	2146.5	R	0.42			*-8.80*	
Ps1115s	2148.5	R	0.32			*-8.81*	
Ps1116da	2149.4	M	1.13	44/56	-9.37	*-8.47*	
Ps1116db	2149.4	D	1.54	62/38	-6.82	*-6.20*	
Ps1117d	2150.7	R	0.16			*-9.54*	
Ps1119s	2152.5	O	1.64			*-6.19*	
Ps1120d	2153.7	O	1.61			*-6.20*	
Ps1122d	2155.4	R	1.38	71/29	-10.10	*-9.64*	
Ps1124g	2157.7	R	2.16			*-9.20*	
Ps1126d	2159.7	R	2.61	67/33	-9.25	*-8.71*	
Ps1128d	2161.7	R	2.96			*-8.87*	
Ps1129_30a	2162.1	D	3.28	57/43	-9.41	*-8.72*	
Ps1129_30b	2162.1	O	2.53	22/78	-6.94	*-5.68*	
Ps1130d	2163.0	D	3.40			*-8.57*	
Ps1132g	2164.4	R	3.91			*-7.78*	
Ps1133_60	2165.7	D	4.02	58/42	-8.44	*-7.76*	
Ps1134s	2166.6	D	4.06			*-8.26*	Reda Mb. top
Ps1135s	2167.6	D	2.19	74/26	-8.10	*-7.68*	
Ps1136_15	2167.9	D	3.41	55/45	-10.59	*-9.86*	
Ps1137_30	2168.7	D	4.12	53/47	-9.33	*-8.58*	
Ps1137d	2169.1	D	2.62	64/36	-11.36	*-10.77*	
Ps1138s	2170.1	R	3.72			*-10.13*	

sample	depth	facies	$\delta^{13}C$	calcite/ /dolomite	$\delta^{18}O$ corrected	$\delta^{18}O$ sample	
Ps1139s	2171.4	R	4.36	71/29	-10.07	*-9.59*	
Ps1139_60	2171.5	D	5.19	43/57	-8.53	*-7.61*	
Ps1140_20	2172.3	C	5.21			*-7.68*	laminated calcisilitites
Ps1140d	2172.8	C	6.60	68/32	-9.19	*-8.68*	
Ps1141s	2173.7	B	7.00			*-8.20*	
Ps1142_30	2174.7	B	8.25			*-7.86*	
Ps1142d	2175.1	B	7.97	76/24	-8.25	*-7.86*	
Ps1143d	2176.1	B	8.24	85/15	-8.20	*-7.96*	
Ps1143dw	2176.2	D	8.06			*-7.51*	
Ps1144dw	2177.0	D	8.09	83/17	-7.34	*-7.07*	
Ps1144d	2177.1	A	7.43	84/16	-8.91	*-8.66*	
Ps1145sw	2177.9	D	7.80			*-7.35*	
Ps1145d	2178.1	B	7.47	82/18	-8.57	*-8.28*	
Ps1146sw	2178.9	D	7.75			*-9.20*	
Ps1146d	2178.9	B	7.67	85/15	-10.98	*-10.73*	
Ps1147d	2179.7	B	7.54	78/22	-8.95	*-8.60*	
Ps1148d	2180.7	B	7.43	77/23	-9.16	*-8.79*	
Ps1149d	2181.7	B	5.80	76/24	-8.79	*-8.39*	
Ps1150d	2182.7	B	5.37	77/23	-9.07	*-8.71*	
Ps1150_80	2182.8	D	5.44	82/18	-8.94	*-8.65*	
Ps1151d	2183.7	A	4.62	84/16	-9.42	*-9.16*	
Ps1152_40	2184.4	B	4.38	80/20	-9.33	*-9.01*	
Ps1152d	2184.7	C	3.99	61/39	-8.55	*-7.92*	
Ps1153_05	2185.1	C	3.11	38/62	-9.85	*-8.85*	
Ps1153_45	2185.5	M	1.33	25/75	-7.93	*-6.71*	Reda Mb. base
Ps1153d	2185.7	C	1.89	29/71	-6.91	*-5.75*	
Ps1154_20	2186.2	M	1.77	23/77	-6.98	*-5.73*	
Ps1154s	2186.5	R	1.89	50/50	-10.09	*-9.28*	
Ps1155_10	2187.1	M	1.00	15/85	-7.62	*-6.25*	
Ps1155s	2187.5	R	1.70			*-7.25*	
Ps1156s	2188.5	R	1.64	46/54	-9.45	*-8.58*	
Ps1157_30	2189.3	M		14/86	-1.40		
Ps1157s	2189.5	R	1.53	53/47	-9.38	*-8.63*	
Ps1158s	2190.5	R	1.20			*-9.15*	
Ps1159_20	2191.2	M	0.71	14/86	-6.43	*-5.04*	
Ps1159_40	2191.3	M	0.97			*-10.61*	
Ps1160_05	2192.2	R	0.94	67/33	-10.92	*-10.38*	
Ps1160s	2192.7	R	1.28	69/31	-10.17	*-9.67*	
Ps1161_05	2193.3	R	1.20	70/30	-10.52	*-10.04*	
Ps1161d	2193.9	R	0.91			*-10.21*	
Ps1161m	2194.0	M		20/80	-1.31		
Ps1163s	2195.7	R	0.66	80/20	-10.74	*-10.42*	
Ps1164_10	2196.3	O		50/50	-0.82		
Ps1165s	2197.7	R	0.41			*-10.29*	
Ps1167d	2200.1	R	0.31	64/36	-10.00	*-9.41*	
Ps1168_15	2200.7	M	-0.04	75/25	-7.32	*-6.92*	
Ps1169_15	2201.9	R	-1.29	63/37	-11.07	*-10.46*	
Ps1169	2202.0	N	0.01			*-9.61*	
Ps1172g	2205.0	R	0.00	64/36	-10.83	*-10.24*	
Ps1172_80	2205.5	M		20/80	-1.31		
Ps1175s	2208.2	R	-0.24	69/31	-10.88	*-10.38*	
Ps1175_80	2208.5	M		25/75	-1.22		
Ps1178_80	2211.5	W	0.79	82/18	-9.08	*-8.79*	
Ps1180_40	2213.1	M		33/67	-1.09		
Ps1180d	2213.4	R	-0.12	69/31	-10.65	*-10.15*	
Ps1185s	2218.2	R	-0.09	33/67	-11.22	*-10.14*	
Ps1190s	2222.5	R	-0.30			*-10.63*	

Table 2. Bulk rock stable carbon and oxygen isotopes and semi-quantitative XRD carbonate composition of the Ludfordian rocks in the Pasłęk IG-1 borehole section.

(VPDB) by assigning a $\delta^{13}C$ and $\delta^{18}O$ values +1.95‰ and -2.20‰ to NBS19. The $\delta^{18}O$ values of samples were corrected using the phosphoric acid fractionation factor given by Rosenbaum and Sheppard (1986), proportionally to the dolomite/calcite ratio obtained with XRD. Reproducibility for the isotopic analysis (1σ) after 10 successive measurements of the NBS19 standard was ±0.03‰ for $\delta^{13}C$ and ±0.07‰ for $\delta^{18}O$. The results are compiled in the Table 2.

Carbon and oxygen isotopes were examined only in bulk rock samples. Mechanical separation of the dolomite component for the isotope analysis (see Kozłowski 2015) was not possible due to its relative low content and very small grain size. For the purposes of estimation of the influence of mineralogical carbonate composition on the bulk carbonate isotope ratios, adjacent samples with contrasting calcite/dolomite ratios (obtained from semi-quantitative XRD)

have been used for model calculation. Estimated $\delta^{13}C$ and $\delta^{18}O$ values for pure calcite and dolomite components were calculated as end-members in the mixing model of two adjacent samples. Due to the obvious inaccuracies of this method, the obtained results are treated as approximate estimations, and used only for estimating the relative influence of dolomite (increasing vs. decreasing values) on the bulk-rock isotope ratios.

RESULTS

Lithology (macrofacies)

The carbonate anomaly of the Reda Member (Text-fig. 2; 2186–2166 m) in the Pasłęk IG-1 borehole section occurs within the thick siliciclastic complex of the distal parts of the Kociewie Formation. In the lower part of the measured interval (2272–2198 m; Text-figs 2B, 3B), the Kociewie Formation is composed of more or less equal proportions of clay-dominated [fine claystones (J) – 2%; laminated claystones (L) – 27%; mudstones (K) – 16%,] and silt-dominated components [silty mudstones (N) – 26%; calcareous heterolites (R) – 10%; siltstones (P) – 12%; silt laminated mudstones (O) – 3%].

The first change leading to the facies anomaly is the gradual appearance of the specific dolomitic mudstone facies (M; Text-figs 2B, 3B), appearing for the first time (2237 m) 51 m below the main anomaly. Facies M shows a varve-like compositional lamination, traces of the presence of fine pyrite and towards the top an increasing presence of specific, very thin red clay laminae. Above 2198 m (12 m below the base of the Reda Member), dolomitic mudstones (M) occur more continuously and are the main fine-grained facies component (23% on average; Text-fig. 2B). Concurrently, in the same interval (2198–2186 m), the participation of siltstone facies distinctly increases (22 to 32% on average), at the expense of other fine-grained facies (J + K + L decreasing from 43 to 19%).

The mass appearance of calcite grains at the base of the Reda Member (Text-figs 2B, 3B; 2186 m) results in the appearance of laminated calcisiltite facies (A–C), which are calcite-bearing textural equivalents of the dolomitic mudstones (M) occurring below. Facies A (calcisiltites), B (laminated marly calcisiltites), and C (laminated calcareous mudstones) were distinguished macroscopically on the basis of the rise in clay content. The facies show a distinct varve-like lamination resulting from compositional variations between laminae and the total absence of bioturbation. The rocks appear grey with a red-violet hue due the admixture of some red pigment to the terrigenous laminae. Laminated calcisiltite facies strongly dominate (A: 22%; B: 51%; C: 7%; 80% in total) in the lower (carbonate-dominating) part of the Reda Member (2186–2173 m), with only a minor participation of dolomitic mudstones (M: 9%) and texturally massive calcisiltites (D: 9%).

The termination of the carbonate-bearing anomaly (Text-figs 2B, 3B; 2173–2166 m) consists of numerous, thick (up to 50 cm) massive calcisiltite (D) beds (27%), dolomitic mudstones (M: 17%), reappearing laminated claystones (L: 40%) and mudstones (K: 14%). The return of the background facies assemblage (interval: 2166–2123 m) is characterised by a distinctly lower contribution of the silt fraction in comparison to the beds immediately below the Reda Member. The complex is dominated by laminated claystones (L: 45%), and mudstones (K: 13%), with subordinate silt laminated mudstones (O: 19%), calcareous heterolites (R: 12%) and rare intercalations of dolomitic mudstones (M: 5%). In the next interval (2123–2050 m), referred by Modliński *et al.* (2006) to the Puck Formation, further decline of the silt facies components proceeds (Text-fig. 2B). At a depth of 2050 m (section measured up to 1990 m), a strong facies shift toward the domination of fine claystones facies (J) is observed.

Updated graptolite biostratigraphy

The existing archival biostratigraphic graptolite data (Tomczyk 1973) precede the novel taxonomy and stratigraphy of the upper Ludfordian graptolite fauna introduced by Tsegelnjuk (1976) and Urbanek (1997). For this reason the graptolite fauna occurring especially above the Reda Member needs to be revised. The Kociewie Formation below the Reda Member contains abundant specimens of *Bohemograptus bohemicus* (Barrande, 1850) and rare *Neocucullograptus* spp. up to a depth of 2200.5 m (Text-figs 2C; 3A). Above this level, the dolomite mudstones – siltstone complex, as well as the Reda Member are almost de-

Text-fig. 4. Thin-section photomicrographs illustrating details of the pre-event facies i.e., immediately below the Lau event interval (below the → Reda Member) in the Pasłęk IG-1 core; colour marks on the photographs indicate the mineral composition: red – quartz, green – mica, blue – calcite, orange – dolomite, orange/red outline – abraded dolomite, black – organic matter, yellow – pyrite. A-B – Changes observed in the laminated mudstone facies, between 2218 m (A) and 2187.5 m (B) (respectively 32 and 1.5 m below the base of the Reda Member; uniform magnification); note the appearance of abundant dolomite silt inside the aggregates (one aggregate is outlined by a white dashed line) toward the top (B); transmit-

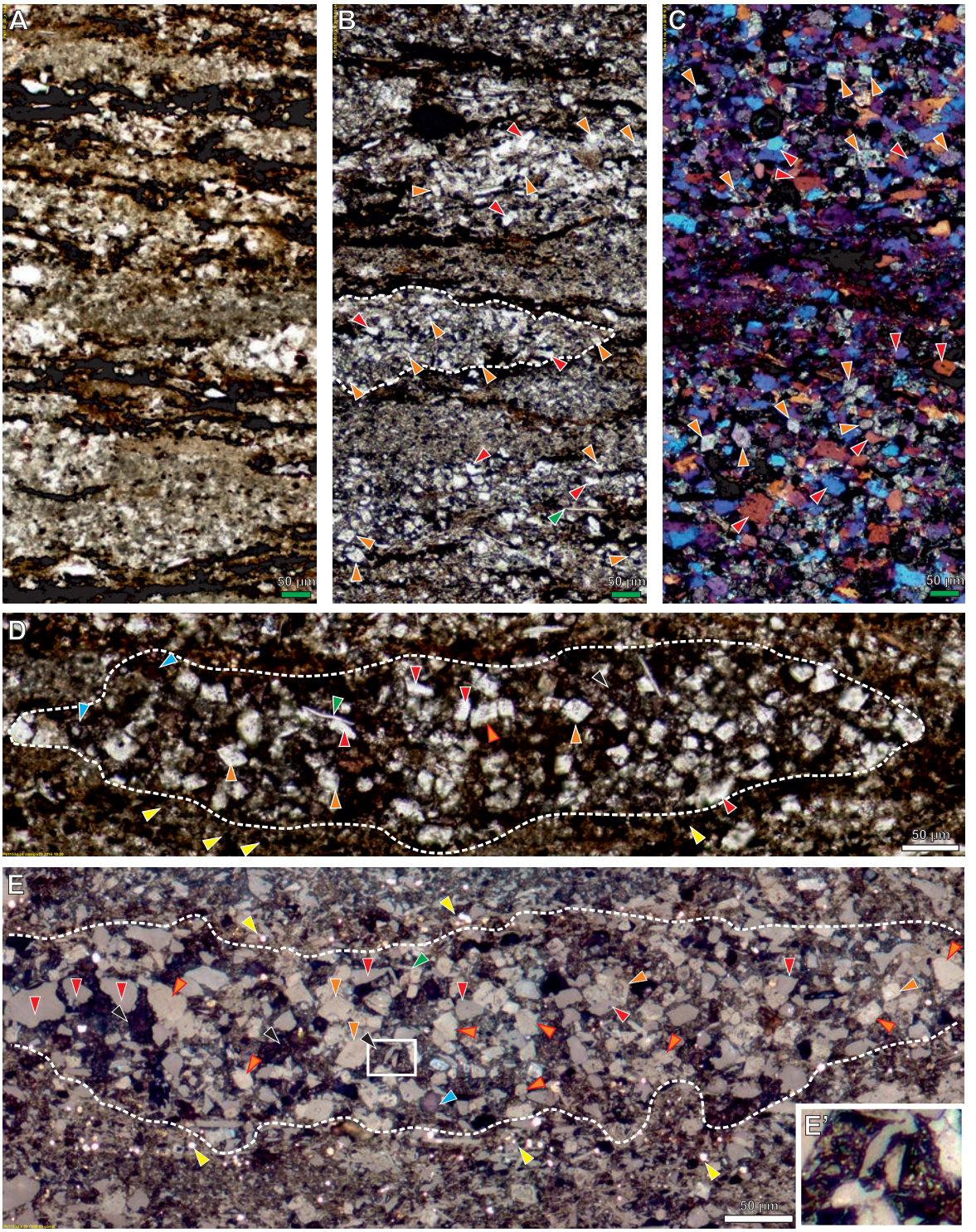

ted light, one nicol; C – Laminated siltstone facies, 0.5 m below the base of the Reda Member, with visible common sorting of quartz and dolomite grains; note that the dolomite grains not exceed 40 µm in size, whereas quartz grains reach up to 60 µm; the clay bearing laminae in the middle contain only minute quartz and dolomite silt grains; transmitted light, nicols crossed (note unusual interference colours due to atypical thin-section thickness); D-E – Rock-forming elongated aggregates of grains just below the base of the Reda Member (depth 2186 m) in transmitted (D) and combined transmitted and reflected light (E); one nicol (stained with Dickson's solution). Opaque binder of aggregates is composed of clay and filamentous organic matter (enlarged in insert E'); note that pyrite preferentially occurs outside the grain-bearing core of the aggregates and minute pyrite grains forming a 'pyrite-halo' around the aggregates (yellow marks, opaque in D and bright dots in E).

void of graptolite macrofossils up to a depth of 2177 m, where sparse fragments of pristiograptids are observed. Above the carbonate-bearing interval, a post-extinction biostratigraphically important graptolite fauna was observed (Text-figs 2; 3A) in a succession typical for the entire Polish Basin (Urbanek 1997) i.e.: *Pseudomonoclimacis latilobus* (Tsegelnjuk 1976) – FO 2156 m; *Slovinograptus balticus* (Teller 1966) – FO 2133; *Uncinatograptus acer* (Tsegelnjuk 1976) – FO 2122 m; and a single point finding of *Uncinatograptus acer aculeatus* (Tsegelnjuk 1976) – FO 2056 m. The topmost part of the Silurian succession in the analysed section contains graptolites of the *Uncinatograptus spineus* group (FO 2010 m) indicating its latest Ludfordian age.

Microfacies and mineral composition

The 'varve-like' laminated facies observed in the event interval (Text-fig. 3B) shows an evolution corresponding to general changes in mineral composition (Text-fig. 3H). The gradual increase of dolomite and quartz silt toward the base of the Reda Member is coeval with the appearance of the dolomitic mudstone facies (M; Text-figs 2C, 3). At the base of the Reda Member, the appearance of calcite transforms facies M into laminated calcareous mudstones (C) and calcisiltites (A, B).

The laminated texture of the dolomitic mudstones (M) results from the appearance of horizontal accumulations of lens-shaped organic-silt aggregates (Text-fig. 4A *vs.* B). The accumulations show sharp bases and tops, with no signs of reworking or erosive base surfaces. Single aggregates (~1 mm long and ~0.1 mm thick) are composed of dolomite, quartz, and muscovite silt (up to 40 μm in size) and are bonded by organic-clay matter (Text-fig. 4D, E). The dolomite crystals show diverse roundness conditions – from almost euhedral crystals to well-rounded grains (Text-fig. 4E – orange/red marks). Fine pyrite framboids are most abundant between the aggregate accumulations in clay-mud horizons. Framboids are sparse in the interiors of aggregates but show local concentrations outside at the aggregate margin, forming a 'pyrite halo' (Text-fig. 4D, E). The subordinate single red-clay laminae consist of fine clayey matrix, with abundant (up to 40%), very fine, individual, distinctly oxidized pyrite framboids; numerous graptolites and organic cyst cross-sections.

The dolomite silt enrichment, below the base of the Reda Member, is also manifested in the coarse-grained facies. The siltstones below the dolomite-mudstone bearing interval (up to 2198 m) are dominated by quartz-mica silt and only in some cases contain carbonates, represented by dispersed, fine biodetritus, blocky calcite cement and rare fine detrital grains. Toward the top – in the event prelude, siltstones become dolomite-rich and show common sorting between quartz and dolomite expressed as clay-silt lamination (Text-fig. 4C) and normal grading inside the laminae. The dolomite crystals show different roundness. Additional blocky dolomite cement between the dolomite grains as well as dolomite-cemented aggregates are locally noted in the dolomite abundance maximum, just below the base of the Reda Member.

The first appearance of non-detrital calcite occurs as a component of silt aggregates in the dolomitic mudstone facies (M). Toward the base of the Reda Member, calcite evolves from single anhedral crystals within aggregates in facies M (Text-fig. 4E – blue mark); through elongated, thin overgrowths-ingrowths (Text-fig. 5A, B) and subhedral bulging growths on the aggregate surfaces (as e.g., the spheroid illustrated in Text-fig. 5C) – in the base of the Reda Member (facies C); to individual calcite rafts (Text-fig. 5D), euhedral grains and thick incrustations of aggregates (Text-fig. 5E) within the Reda Member. The distinct calcite enrichment (according to XRD data – Text-fig. 3H), starts at the base of the laminated calcisiltite facies interval and causes dilution of detrital components. Concurrently, the dolomite contribution to the detrital material (dolomite normalized to dolomite + quartz + feldspar) attains the maximal level across the 'sparoid'-bearing interval.

The main, rock-forming components in the calcisiltite facies of the Reda Member are characteristic calcite grains referred as 'sparoids', described earlier in detail in the Reda Member of the Mielnik IG-1 section (Kozłowski 2015; no. 14 in Text-fig. 1). Compared to that case, the calcite grains in the Pasłęk-IG1 section are more complex and occur as successive micromorphologic types. The most primary type ('cloudy sparoids') consists of individual euhedral to subhedral equant calcite crystals (10 to 50 μm in size), with a dominant rhombohedral morphology. The crystal centres contain anhedral clouds of filaments (Text-fig. 6A–C, F) in the shape of empty nanotubes (e.g., Text-fig. 6D, F, G). The cloudy centres are overgrown by limpid calcite up to an euhedral crystal shape (Text-fig. 6F; and also A, B, C, G). The outside veneers of the crystals are sometimes unstained (Text-fig. 7C), recognised in SEM-EDS as a Mg-enrichment. The cloudy sparoids, beside individual crystals (as e.g., in Text-fig. 6B, lower part), form crystal clusters or series, developed

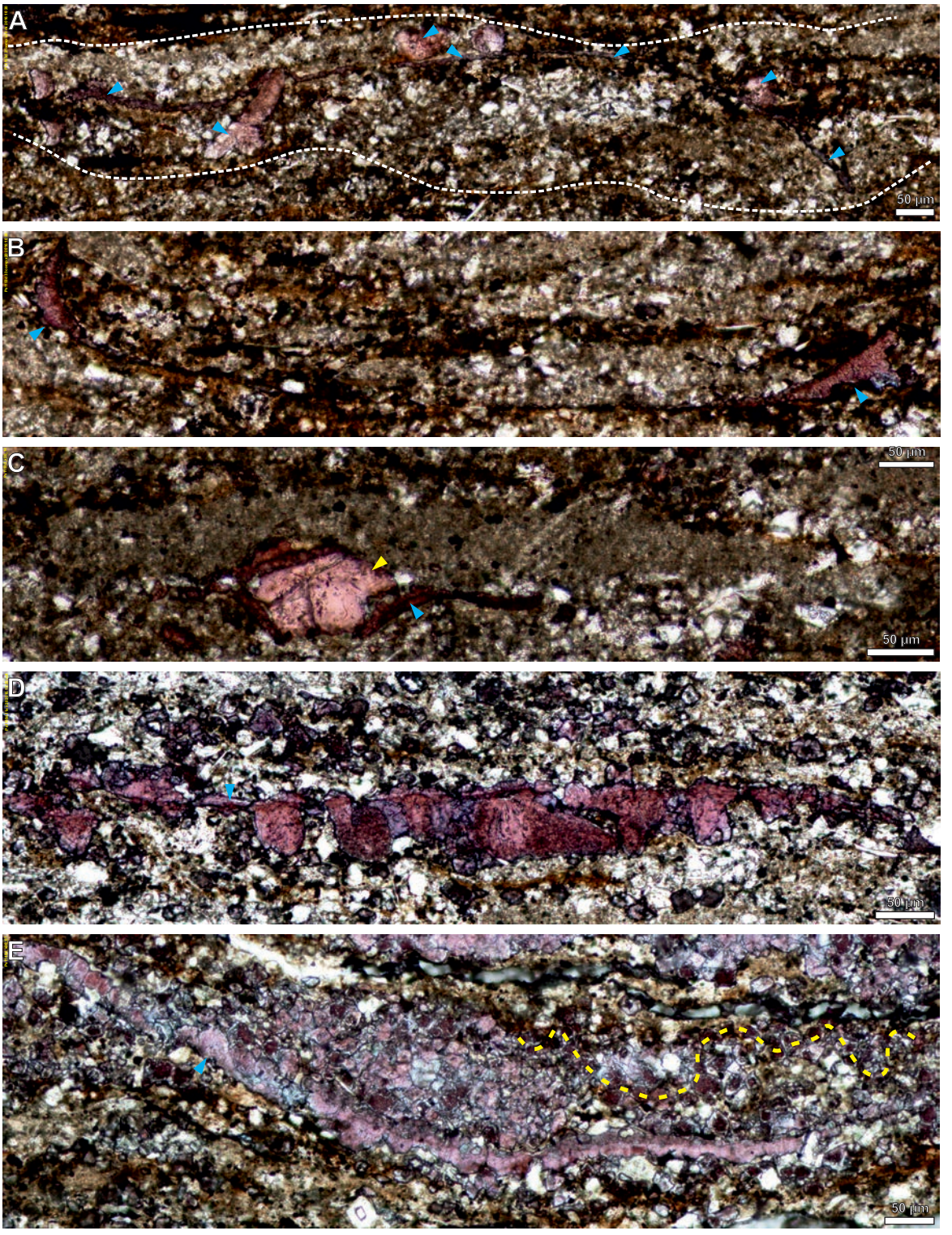

Text-fig. 5. Thin-section photomicrographs illustrating initial appearance and later development of calcite precipitate growths (blue marks, stained in pink), which evolved in the succession from incrustations or ingrowths of non-carbonate grain aggregates (A-C) at the base of the Reda Member (2185.7 m); to one-side growing individual calcite rafts (D – 2183 m); and incrustations of calcite grain aggregate (E – 2181 m) in the middle part of the member; note sparoid spherulite growing on organic-clay aggregate in C (yellow mark); and transition between calcite bounded 'rigid' flake (E – centre) into organic matter bounded aggregate sector with sparoid chain on the right (yellow dashed line); all samples stained with Dickson's solution, transmitted light, one nicol.

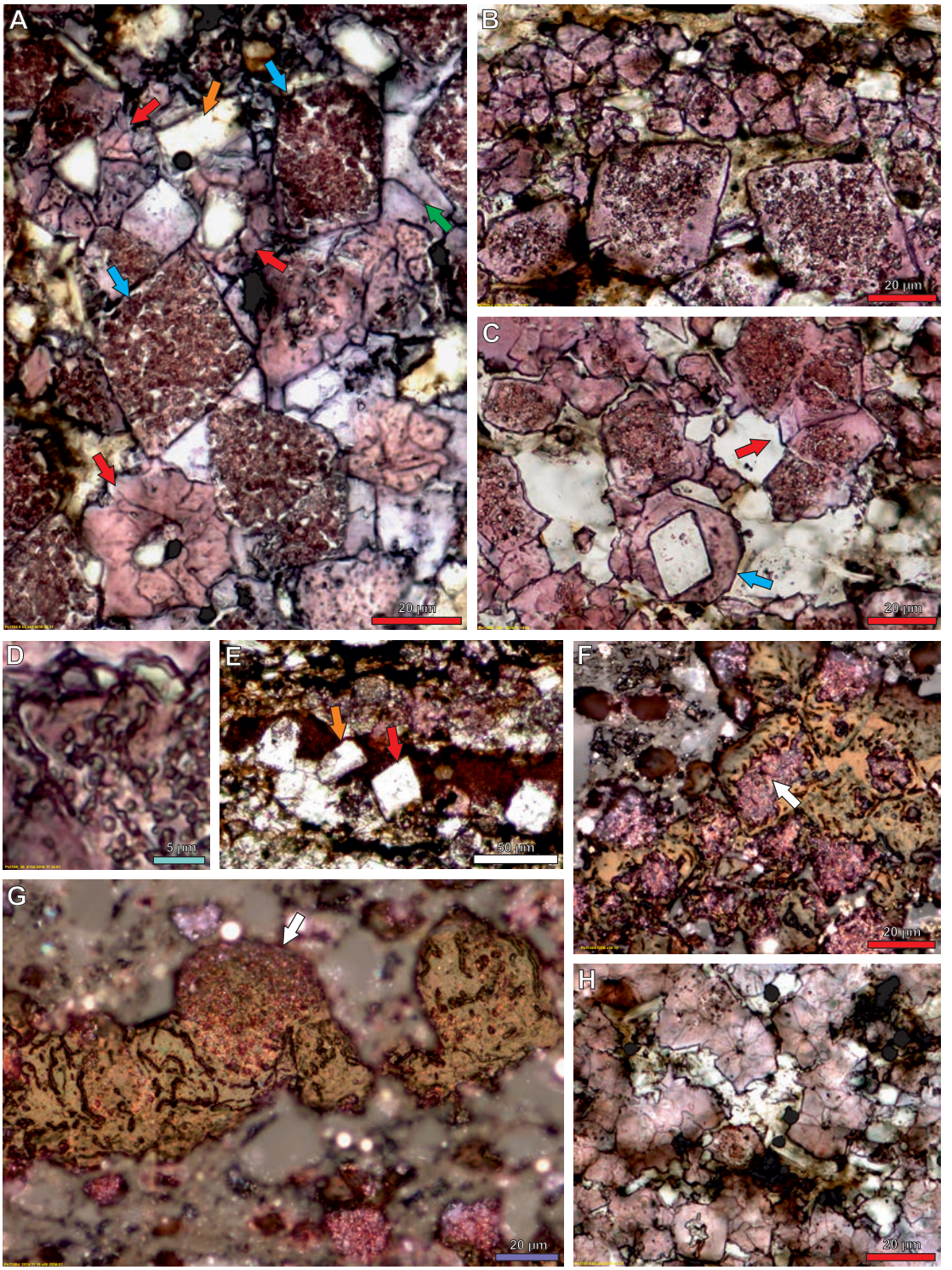

Text-fig. 6. Thin-section photomicrographs illustrating details of calcite 'sparoids' anatomy in the Lau event (Reda Member) interval. A – Blue arrows: rhombohedral, euhedral cloudy calcite crystals, including numerous empty nanotube moulds – interpreted as spaces after entombed filamentous picocyanobacteria; red arrows: sub- to anhedral limpid calcite spheroids formed around tiny detrital (quartz, dolomite) grains; the sparoids and dolomite (orange arrow) are cemented into aggregates by anhedral limpid calcite cement (green arrow); B – Rhombohedral, euhedral calcite grains comprising nanotube moulds; in upper part of the photograph similar filaments bind finer subhedral-limpid calcite and dolomite grains into elongated chain; C – Blue arrow: single coated grain formed by anhedral, limpid calcite overgrowing euhedral dolomite; red arrow: encirclement of subhedral calcite sparoids around single euhedral dolomite grain (compare with spheroids arrowed in A); note →

around detrital (dolomite, quartz) grains in the form of encirclements (Text-fig. 6C – red arrow). In other cases, individual cloudy sparoid series are arranged in long chains (Text-fig. 6B, upper part, 7D), often along the organic matter (OM) relicts. These 'sparoid chains' are perceived as the intersections of three-dimensional fragments of biofilm flocs inlaid with the sparoids. The anhedral cloudy calcite may also overgrow single detrital grains (Text-fig. 6E).

The second category (geometrically probably younger) of the primary calcite grains are limpid crystals locally containing single, larger organic filaments (Text-fig. 6G). The limpid calcite often forms ovoid overgrowths around detrital (dolomite) grains (Text-fig. 6C, blue arrow), or intergrowths with cloudy sparoids (Text-fig. 6G). Commonly, subhedral limpid crystals are clustered radially around detrital grains forming spheroids (Text-fig. 6A, C, red arrows) or growing radially as spherulites around tiny (?organic) opaque centres (Text-fig. 6H). A large part of the 'cloudy' and 'limpid' sparoids is gathered in individual aggregates (100 to 300 μm in size; Text-fig. 7), often organised around (Text-fig. 7B) or assembled with the detrital grains (Text-fig. 7C). The 'primary' sparoids are agglomerated with relicts of OM into 'loose' flocs (Text-fig. 6B, upper part; Text-fig. 5E, right part of aggregate – dashed line) or bonded by anhedral limpid calcite cement (Text-figs 6A, 7A), containing single organic filaments (green arrow in 7A) into 'rigid' calcite flakes. The latter sometimes contain, preserved inside, 'primary' sparoids in an original arrangement (e.g., chains composed of cloudy euhedral grains – Text-fig. 7D). Some of the aggregates are additionally attached to calcite rafts (Text-fig. 7F) or overgrown by calcite incrustations (Text-fig. 5E).

The primary 'sparoid' individual grains and/or their aggregates (both flocs and flakes) are texturally arranged into 'varve-like' laminated calcisiltite (facies A, B, C) or massive calcisiltite (facies Da, Db). The 'varve-like' texture is formed by parallel bands of individual (Text-fig. 8A) and/or aggregated 'sparoids' (Text-fig. 9A), with relative dilutions of detrital grains, clay and pyrite framboids, compared to adjacent continuous clay-terrigenous horizons (containing only single 'sparoids'). The 'sparoid' bands lack any erosive bases nor have any internal signs of horizontal transport (imbrication, cross-arrangement). The wavy geometry results from commonly undulate bases and lateral thickness variations.

More continuous laminae are dominated by individual (non-bonded) 'primary' grains (Text-fig. 8A) and locally show normal gradation (Text-fig. 8B–D), with larger euhedral sparoids and single clusters (e.g., spheroids, chain fragments) accumulated close to the base, and fine subhedral individual 'sparoids' in the top. The bases of such laminae contain micro-load cast structures (Text-fig. 8B, C). The well-sorted grainy laminae are often cemented by final (diagenetic) generation of anhedral calcite cement (Text-fig. 8C, D). The discontinuous bands are composed mainly of individual disconnected to coalescent floc and flake sparoid aggregates (outlined in Text-fig. 9A). The latter show truncated discontinuous cement and/or are overgrown by calcite incrustations.

The 'varve-like' facies in the anomaly climax contain several exceptionally thick (reaching up to 5 mm) laminae with various, often unique internal textural arrangements. The first textural variation (Text-fig. 10A) is arranged from normally-graded flocs, combined with gradation of individual large single sparoids and very fine sparoid grains in the lamina top. The second type (Text-fig. 10B, C) shows a chaotic arrangement of soft-deformed, elongated sparoid flocs with partitions of clay-organic matter in between. The third variation is very similar to the textural arrangement of the Db facies (see below), and shows a chaotic arrangement of long convoluted sparoid chains and encirclements, along with the domination of dolomite and mica within the clastic component (Text-fig. 10D).

Beside the laminated facies (A–C), the sparoid grains occur as a component of the calcisiltites with a massive texture (facies D; Text-fig. 9B–E). The beds are 2–100 mm thick and occur inside the 'varve'-like marlstone bedsets or in the prelude of the terrigenous intercalations (see Text-fig. 3B). Macrofacies D occurs as two microfacies (Da, Db). Microfacies Da (Text-fig. 9B) forms normally-graded beds, with vertical separation (demixing) of the components and an abrupt, undulate (erosive) base preserved (Text-fig. 9B). The lower part of the beds contains a dense

the occurrence of an anhedral, limpid dolomite (unstained) cement between the sparoid grains; D – Empty moulds after microbial filaments; E – Euhedral (red arrow) and abraded (orange arrow) dolomite grains incorporated in cloudy anhedral calcite raft flake; F – Cloudy center of sparoid formed by floc of (?cyanobacterial) filament moulds (arrowed, pink), syntaxially overgrown to euhedral shape by limpid calcite (yellow); G –Subhedral cloudy calcite sparoids containing nanotube moulds (pink, arrowed) overgrown by sub- to anhedral limpid calcite with entombed larger (?cyanobacterial) filament moulds (black); H –Calcite spherulites comprising tiny opaque nuclei coated with radially arranged subhedral limpid calcite crystals; note the example case of occurrence of the anhedral, limpid dolomite (unstained) cement between the sparoid grains; all samples stained with Dickson's solution; A-E, H – transmitted light, one nicol; F-G – combined transmitted-reflected light, one nicol.

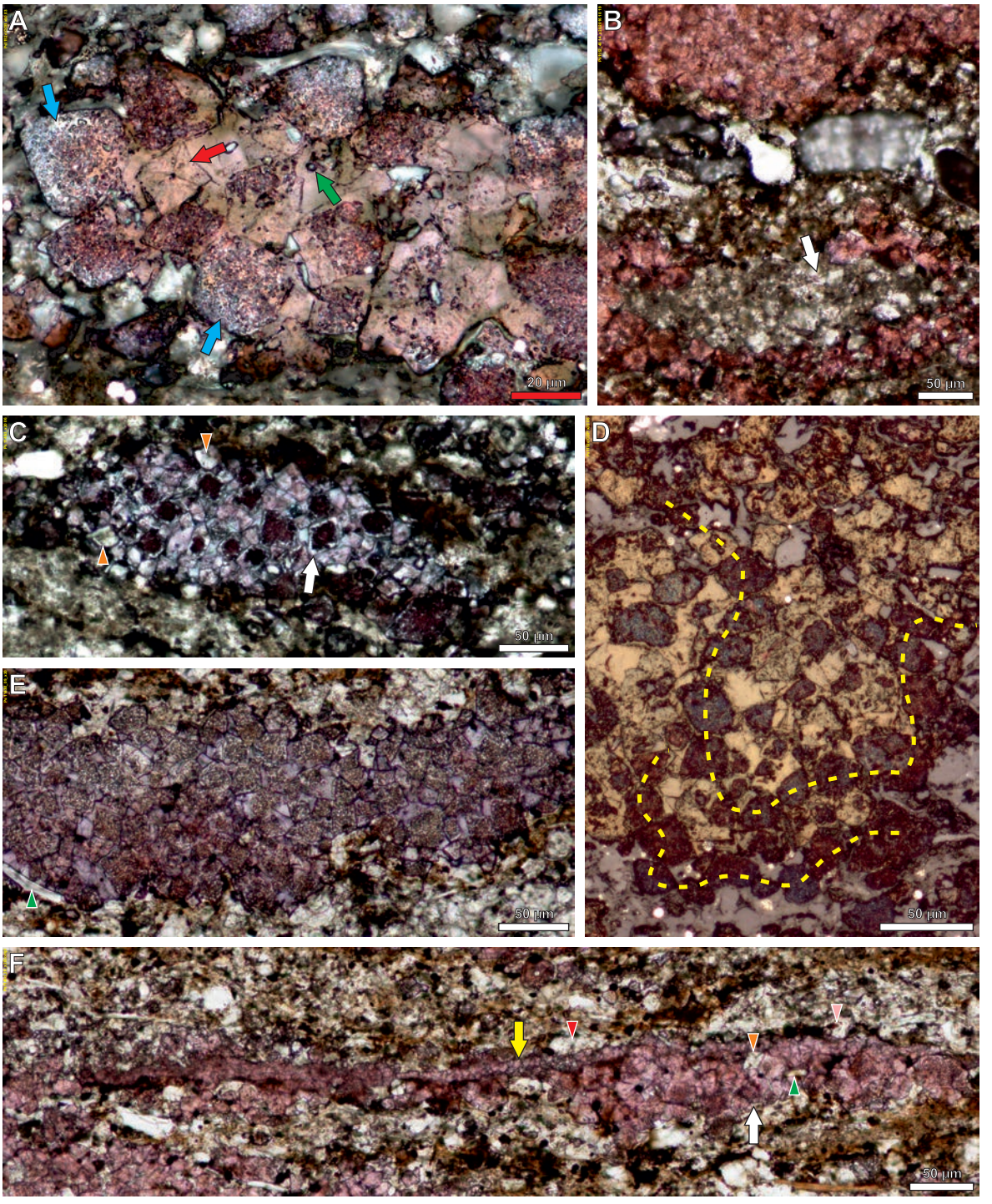

Text-fig. 7. Thin-section photomicrographs illustrating details of sparoid aggregates bonded by anhedral calcite cement (calcite flakes) in the Lau event (Reda Member) interval: A – Eu- to subhedral cloudy sparoids with filament moulds (blue arrow), locally syntaxially overgrown by limpid calcite; and sub-anherdal mainly limpid calcite spherulites (red arrow) – all bound together by anhedral limpid (only single filaments – green arrow) calcite cement into individual rigid calcite flake; B – Aggregate composed of detrital grains (arrowed) encircled by calcite sparoids; C, E – Individual, rigid sparoid flakes (compare with A), composed of rhombohedral, euhedral sparoids, dolomite (orange marks) and mica (green mark), bounded by calcite anhedral cement; note numerous sparoids with cloudy centers and unstained (Mg-enriched) external lattices in C (arrowed); D – Chains (yellow dashed lines) of euhedral cloudy sparoids (burgundy-red stained), fixed by limpid sub-anhedral calcite cement; F – White arrow: rigid sparoid flake composed of eu- to subhedral cloudy calcite sparoids, single euhedral dolomite (orange mark) and mica (green mark), bonded by anhedral limpid calcite cement; the flake is attached to the elongated calcite raft (yellow arrow) with →

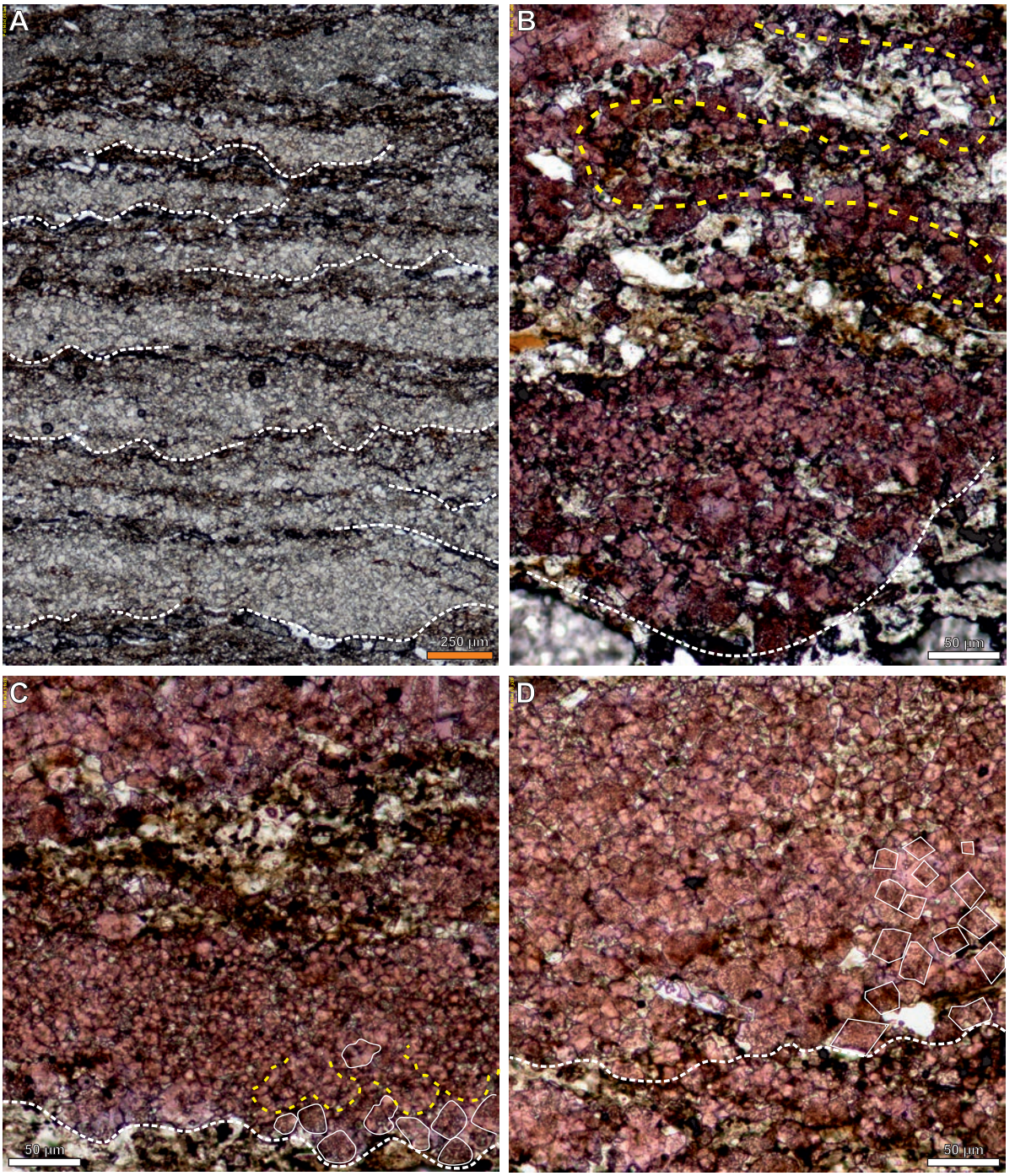

Text-fig. 8. Thin-section photomicrographs illustrating details of textural arrangement in the laminated calcisiltite (sparoid) facies in the Lau event (Reda Member) interval. A – Laminated calcisiltite (facies A) composed of calcite laminae (light) dominated by individual 'sparoids'; separated by clay-detrital darker laminae; white dashed lines highlighting undulate bases of the calcite-bearing laminae (micro load cast structures); B – Lower part: details of micro load cast structure (white dashed line) at the base of the internally graded lamina; upper part: chaotic sector with sparoid chain – yellow dashed line; C, D – Laminae of calcite sparoids showing undulate bases (dashed lines) and internal normal grading (part of single, large sparoids in the lower part is outlined by solid lines, yellow dashed lines highlight sparoid chains); all samples: transmitted light, one nicol; B-D: stained with Dickson's solution.

adhered quartz (red mark) and dolomite (pink mark) at its top surface; all samples stained with Dickson's solution; B, C, E, F – transmitted light, one nicol; A, D – combined transmitted-reflected light, one nicol.

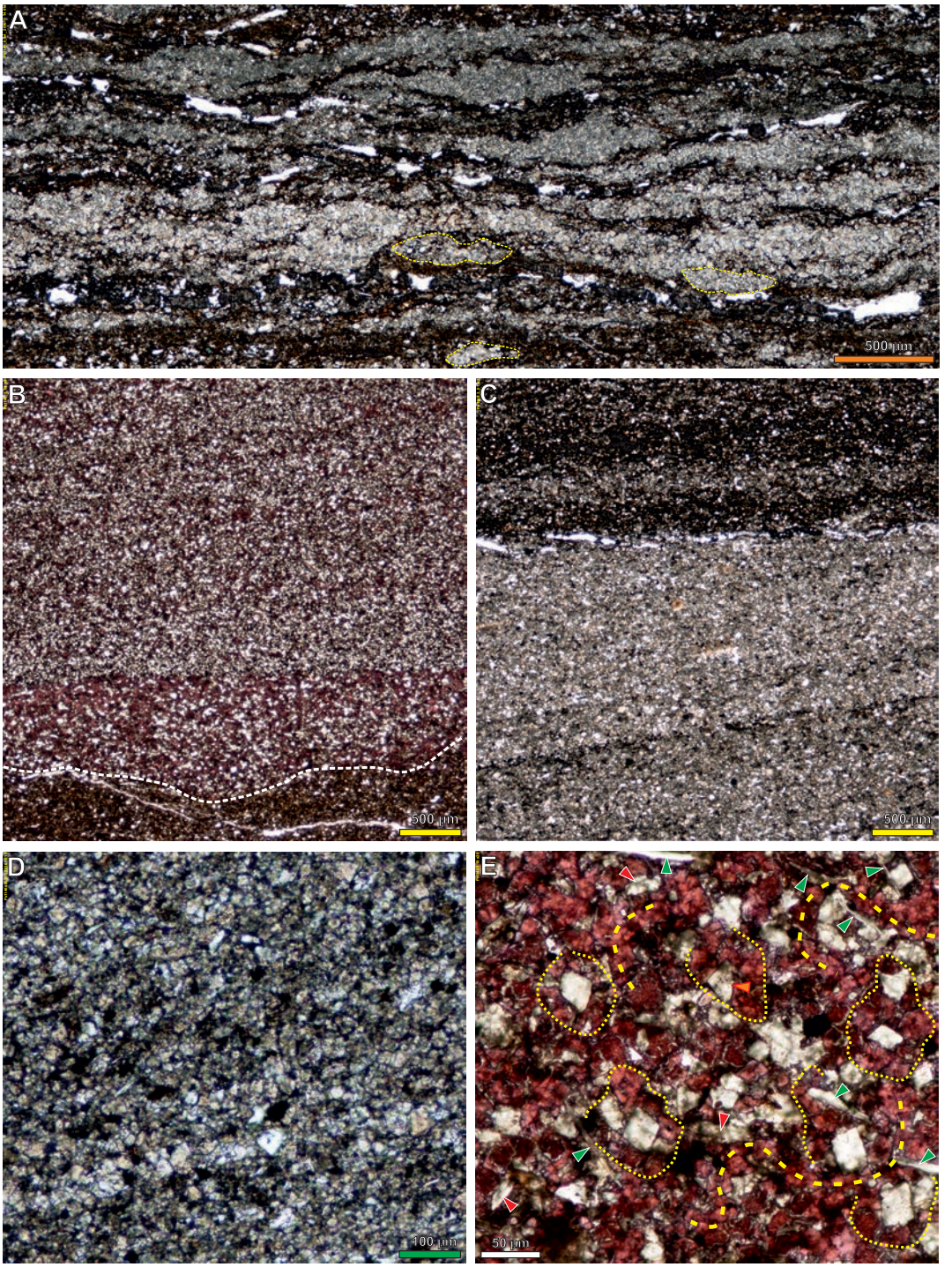

Text-fig. 9. Thin-section photomicrographs showing aspects of textural arrangement in the 'sparoid' facies in the Lau event (Reda Member) interval. A – Laminated marly calcisiltite facies (facies B) composed of calcite bands (light) dominated by individual and/or coalescent sparoid aggregates (examples are outlined by yellow dashed lines); B – Massive, clastic-bearing calcisiltite facies (Da), showing sharp based (dashed line) graded bedding with demixing of coarser carbonate sparoids (on the base) and finer clastic material (toward the top) with low angle cross lamination; C, D – Massive, pure-carbonate calcisiltite facies (Db), showing cross-bedding in lower part (C, enlarged in D), and parallel lamination in the upper part (C); E – Details of the massive, pure-carbonate calcisiltite facies (Db) consist of numerous sparoid encirclements (outlined by yellow dotted lines) around euhedral to abraded (orange mark) dolomite grains; and sparoid chain (yellow dashed lines); note that detrital grains are represented mainly by dolomite and mica (green marks) with relative underrepresentation of quartz (red mark); all samples: transmitted light, one nicol; B, E – stained with Dickson's solution.

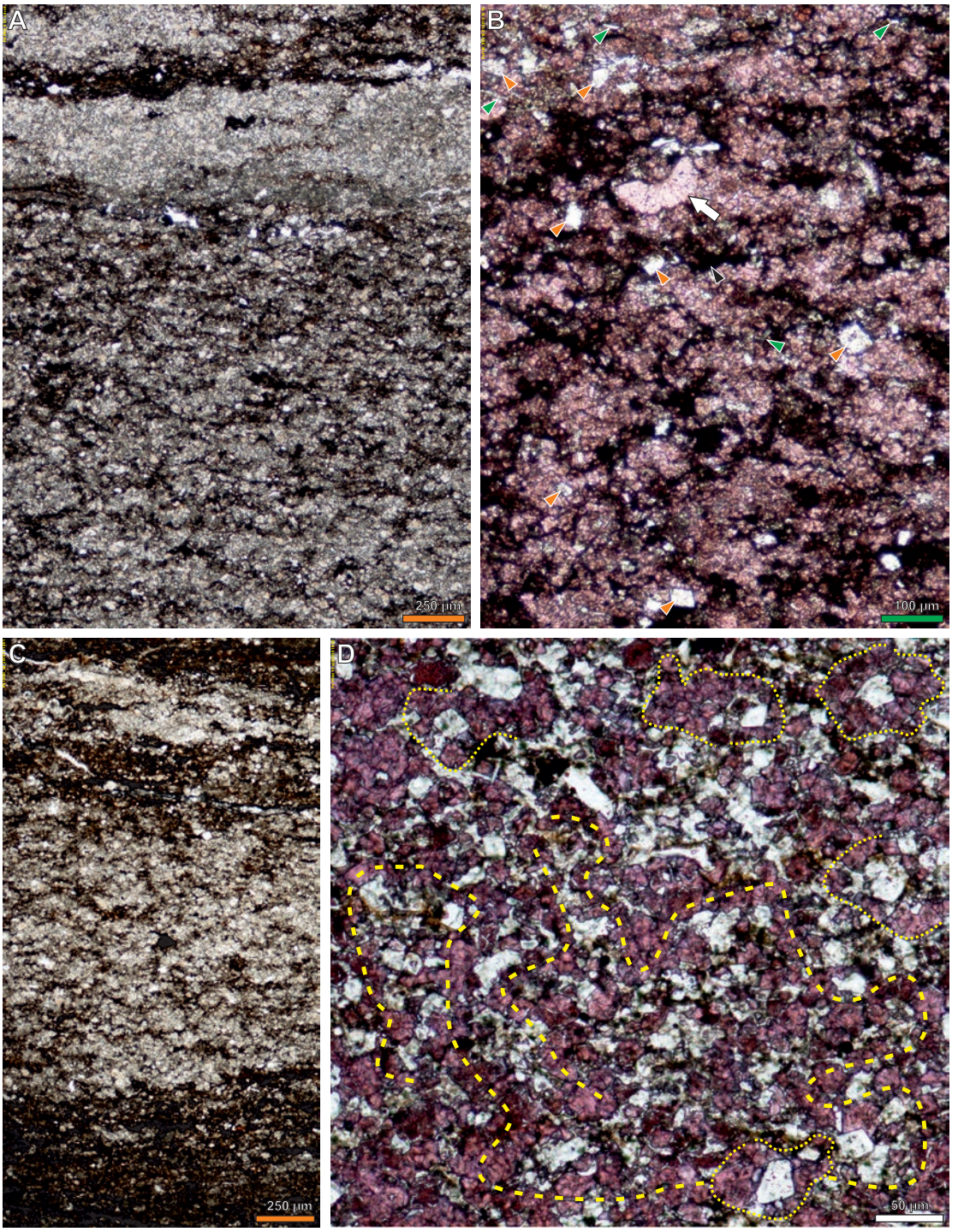

Text-fig. 10. Thin-section photomicrographs illustrating details of texture of thick, laterally continuous laminae, with internal 'chaotic' or 'graded' flocs arrangement in sparoid facies in the Lau event (Reda Member) interval. A – Exceptionally thick calcite-bearing lamina showing normal grading of floc aggregates, combined with inverse gradation of loose individual sparoid grains, covered in the top by finest grains accumulation; B – Chaotic texture of thick laminae (showed in C) composed of soft-deformed elongated sparoid flocs with organic matter agglomeration in-between (black marks); note that detrital grains are represented mainly by abraded dolomite (orange marks) and mica (green marks); larger biogenic grain (arrowed) is probably a fragment of alga; C – Lamina with 'chaotic' texture, with internal separation of calcite flocs by clay-organic matter partitions; D – Anatomy of 'chaotic' texture, containing tangled long sparoid chains (yellow dashed line) and single detrital grains (mainly dolomite) enclosed in sparoid encirclement frames (yellow dotted lines); all samples: transmitted light, one nicol; B, D: stained with Dickson's solution.

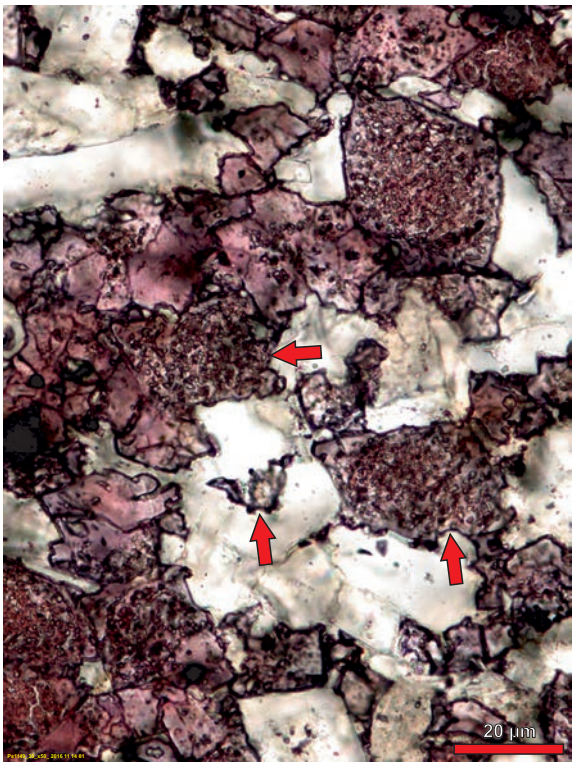

Text-fig. 11. Thin-section photomicrograph illustrating details of sub-vertical dissolution paths along detrital grains (mainly dolomite) filled by secondary dolomite cement; red arrows indicate dissolute sparoid surfaces; transmitted light, one nicol, stained with Dickson's solution.

'sparoid'-dominated accumulation, with some aggregates (chains, encirclement) at the base, covered by a fine-grained, pyrite horizon. The unit is succeeded by a several times thicker well-sorted, low-angle cross-laminated, normally-graded silt (quartz, mica and subordinate dolomite), and containing only accessorial (up to 10%) finer sparoid bands. The top of the succession shows a gradual transition (sometimes with an amalgamation surface) into thick fine mudstones (macroscopically: facies N). The average composition of this variant of facies D seems to correspond to the virtually averaged composition of the laminated marly calcisiltite (facies B–C).

Microfacies Db (Text-fig. 9C–E) consists of a strong domination of 'sparoids' with only accessory detrital dolomite, mica and a relatively under-represented quartz and pyrite content. The beds are low-angle cross-laminated to texturally massive (Text-fig. 9C, D). The 'sparoids' are chaotically arranged and mainly represented by well-preserved encirclements of detrital grains and 'sparoid' chains (Text-fig. 9E). Relatively abundant vase-shaped microfossils (interpreted as tintinnids), are noted in the upper part of the beds. The composition of Db facies shows a distinct enrichment of 'sparoids' and microfossils in relation to the averaged composition of the 'varve'-like marls and strong depletion of quartz in relation to dolomite and mica detrital grains.

The massive, grained sparoid accumulations, occurring in microfacies Db, as well as inside the laminae with an internal 'chaotic' arrangement (in the context of facies A–B), locally contain traces of partial dissolution of calcite sparoids, occurring along sub-vertical paths running along detrital grains (Text-fig. 11). The resulting (often connected) porosity is succeeded by precipitation of the neomorphic dolomite cement (see also Text-fig. 6C, H), regarded as the last generation of carbonate components.

Pyrite framboid size distribution

In the entire studied interval, pyrite occurs as individual micro-framboids, composed of spherical, densely packed, octahedral – euhedral microcrystals. The original mineralogy is very well-preserved, but inside the red clay laminae (facies M) very abundant pyrite framboids are in the majority altered to goethite, whereas framboids beyond the laminae show no signs of oxidation. The framboid distribution within a single bed is not homogenous – with strong depletion inside the grain aggregates or accumulations (both 'sparoid' and detrital), contrasting with a distinct pyrite enrichment in the clay component (especially the red-coloured bands). Locally, the framboids form disconnected groups, especially observed around aggregates or inside the red-clay laminae. The measured and calculated statistical parameters of the framboid populations are listed in Table 1 and visualised on the diagrams (Text-figs 3E and 12).

The statistical parameters plotted onto diagrams, proposed by Wilkin *et al.* (1996), allow five (sub-) types of pyritization (see Text-fig. 12 and Table 1) to be distinguished, distributed consistently with the facies pattern (Text-fig. 3E). The most extreme subtype referred here as "A1–A2" appears with facies M, at a strong increase of detrital dolomite admixture (Text-fig. 3E, Table 2), 8 meters below the base of the Reda Member and occurs continuously across the whole 'sparoid' anomaly (facies A–C). The "A1–A2" pyritization type shows: a minimum mean diameter of framboids (below 3.85 and 4.2 µm, respectively), minimum standard deviations (below 1.33 and 1.57 µm, respectively), lowest skewness (between 1.0 and 1.5), strong dominance of framboids below 5 µm

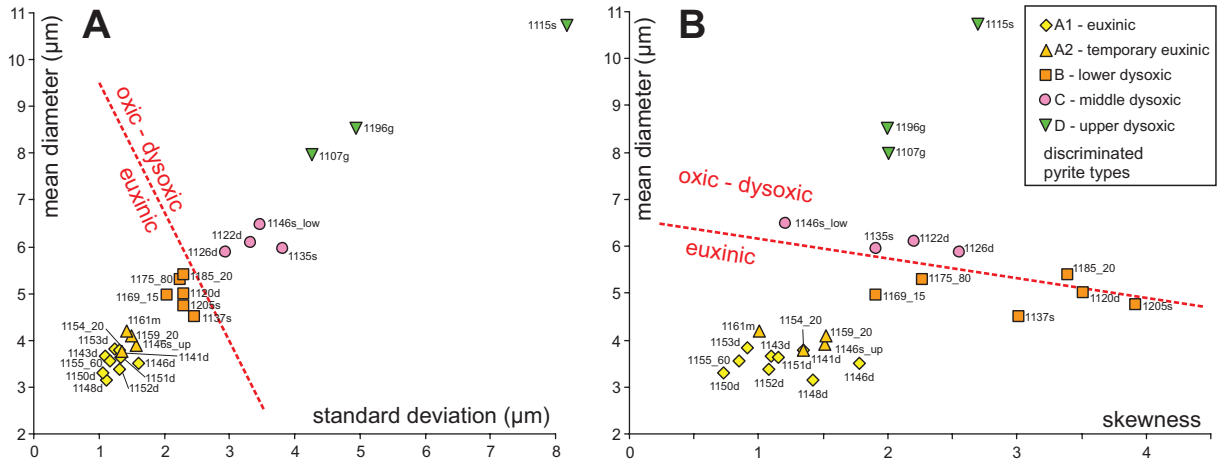

Text-fig. 12. Statistical parameters of pyrite framboid diameters on discrimination plots (plots and discriminate fields after Wilkin et al. (1996): A – mean diameter vs. standard deviation; and B – mean diameter vs. skewness plots; A–D: discriminated pyritization type suits interpreted as recording various redox conditions in the sediment-water column.

(82–93% and 73–82% of all framboids) and virtual absence of framboid coalescence and overgrowing, as well as framboids larger than 10 µm in diameter (single horizontal occurrences in A2 type). At the base of the 'sparoid' anomaly occurs a twofold depletion in pyrite content (from c. 5‰ to below 2.5‰; Text-fig. 3E), visually related to calcite dilution (calcite bands are almost pyrite-free). The pyrite framboids occurring outside the carbonate anomaly (Text-figs 3E and 12) show: (1) larger average and median sizes in framboid diameter; (2) high contribution of framboids with diameters above 5 µm; (3) moderate standard deviation and skewness of framboid diameter; and (4) larger maximum framboid diameters (40 µm below, and 30 µm above the anomaly, respectively).

Isotope record

The isotope record of the studied interval was examined in the bulk-rock carbonate component, composed of calcite and dolomite phases. Despite the expected suppression by some accessory detrital dolomite admixture (Kozłowski 2015), the mid-Ludfordian Carbon Isotope Excursion (CIE) in the Pasłęk IG-1 borehole section is pronounced, well-defined and (surprisingly) reaches a very high magnitude, comparable only with the mid-Ludfordian CIE values recorded in the shallow-water carbonate platform interiors (Text-figs 2D, 3C; Table 2). The core of the excursion in general is coeval with the Reda Member carbonate facies anomaly.

The performed paired analysis (adjacent dolomite *vs.* calcite rich samples; see Text-fig. 13) allows for monitoring the influence of the accessory dolomite component on the bulk-rock record. The (negative) correlation between the dolomite contribution and bulk rock $\delta^{13}C$ values is absent below the event prelude interval up to depth 2189 m ($R^2 = 0.000002$) and insignificant in the anomaly climax interval (2185–2172 m; $R^2 = 0.015$); whereas it shows moderate significant correlation in the event prelude interval (2189–2185 m; $R^2 = 0.72$) and in individual sample pairs in the interval of the decreasing limb of the anomaly (above 2172 m). In the event prelude and CIE decreasing intervals, adjacent beds with a contrasting calcite/dolomite ratio co-occur, which allows for the approximation of isotope signatures of both components (paired analysis). Contrarily, in the CIE climax, constant dominance of calcite determines the isotope record but also impedes the estimation of accessory dolomite isotope signatures.

The record of the mid-Ludfordian CIE (Text-fig. 3C) starts from a consistent plateau with constant bulk rock values around 0‰ (*vs.* VPDB), noted regardless of the dolomite/calcite ratio (Text-fig. 13). The gradual increase starts just above the last appearance of the *Neocucullograptus–Bohemograptus* graptolite fauna assemblage (*kozlowskii* event at a depth of 2201 m). Above this level, the gradual increase of bulk rock $\delta^{13}C$ values from ~0‰ up to the ~1.9‰ is coeval with the appearance of the 'sparoid' incrustations on detrital aggregates, with estimated model $\delta^{13}C$ values for calcite around 2–3‰. In the same interval, dolomite seems to have lower $\delta^{13}C$ values between 0 and 2‰ (Text-fig. 13). The appearance of single loose sparoids (depth 2185.7 m) is coeval

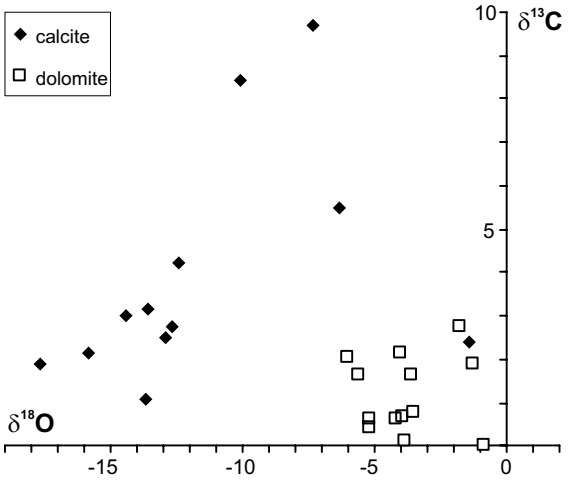

sample pairs	depth	calcite/ /dolomite	measured bulk rock δ13C	measured bulk rock δ18O	calculated (model) calcite δ13C	calculated (model) calcite δ18O	calculated (model) dolomite δ13C	calculated (model) dolomite δ18O*
Ps1111g	2144.3	53/47	0.5	-7.9				
Ps1111_65	2144.6	20/80	1.5	-6.9	-0.9	-9.3	2.2	*-4.0*
Ps1116da	2149.4	44/56	1.1	-8.5				
Ps1116db	2149.4	62/38	1.5	-6.2	2.4	-1.4	0.1	*-3.8*
Ps1129_30a	2162.1	57/43	3.3	-8.7				
Ps1129_30b	2162.1	22/78	2.5	-5.7	4.2	-12.5	2.1	*-6.0*
Ps1139_60	2171.5	43/57	5.2	-7.6				
Ps1140d	2172.8	68/32	6.6	-8.7	8.4	-10.0	2.8	*-1.7*
Ps1140d	2172.8	68/32	6.6	-8.7				
Ps1143d	2176.1	85/15	8.2	-8.0	9.7	-7.3	0.0	*-0.9*
Ps1152_40	2184.3	80/20	4.4	-9.0				
Ps1152d	2184.7	61/39	4.0	-7.9	4.8	-10.2	2.7	*-8.8*
Ps1152d	2184.7	61/39	4.0	-7.9				
Ps1153_05	2185.1	38/62	3.1	-8.8	5.5	-6.3	1.7	*-5.6*
Ps1153_45	2185.5	25/75	1.3	-6.7				
Ps1154s	2186.5	50/50	1.9	-9.3	3.0	-14.4	0.8	*-3.5*
Ps1153d	2185.7	29/71	1.9	-5.8				
Ps1154s	2186.5	50/50	1.9	-9.3	1.9	-17.7	1.9	*-1.2*
Ps1154_20	2186.2	23/77	1.8	-5.7				
Ps1154s	2186.5	50/50	1.9	-9.3	2.1	-15.8	1.7	*-3.6*
Ps1154s	2186.5	50/50	1.9	-9.3				
Ps1155_10	2187.1	15/85	1.0	-6.2	3.2	-13.6	0.6	*-5.1*
Ps1155_10	2187.1	15/85	1.0	-6.2				
Ps1156s	2188.5	46/54	1.6	-8.6	2.7	-12.6	0.7	*-4.0*
Ps1157s	2189.5	53/47	1.5	-8.6				
Ps1159_20	2191.2	14/86	0.7	-5.0	2.5	-13.0	0.4	*-5.1*
Ps1159_20	2191.2	14/86	0.7	-5.0				
Ps1160_05	2192.2	70/30	0.9	-10.4	1.1	-13.7	0.6	*-4.2*

Text-fig. 13. Plot of the carbon and oxygen isotope ratios* of model calcite and dolomite components, obtained from the calculations (below) using paired bulk rock analysis and XRD derived calcite/dolomite ratio. * for calcite-dolomite isotope comparison, the oxygen isotope ratios of dolomite are corrected (-2.6‰) due different fractionation factor during common calcite and dolomite precipitation (Vasconcelos *et al*. 2005).

with the rapid isotope changes. Bulk rock $\delta^{13}C$ values of ~1.9‰ regardless of the dolomite/calcite ratio at the base of the CIE indicate similar and relatively low (~2‰) $\delta^{13}C$ values of both components. Immediately above, across the base of the mass-sparoid facies, the bulk rock values show a rapid pronounced positive shift from 1.89 to 3.11‰, indicating calcite as the main mineralogical carrier of the heavy $\delta^{13}C$ signatures. The increasing limb of the excursion continues in the lower 5 m of the Reda Member carbonate facies anomaly, reaching the CIE maximum plateau at a depth of 2181.5 m (Text-fig. 3C) in the facies where calcite strongly dominates over the dolomite component (Table 2). The maximum plateau (S-Zone of Frýda and Manda 2013) with $\delta^{13}C$ values between 7.43–8.25‰ extends for the next 7 m thick interval up to a depth of 2174.5 m. Assuming the negative influence of the dolomite admixture on the bulk rock $\delta^{13}C$ values observed earlier in the Reda interval of the Mielnik IG-1 section (Kozłowski 2015), the maximum $\delta^{13}C$ values of sparoid calcite are expected to be heavier (probably up to +10‰).

The decreasing limb of the CIE starts within the last 1 m of the laminated calcisiltite complex (Text-fig. 3C), coinciding with the recovery of graptolite fauna, and continuing through the next 5 m within the massive calcisiltite interval. The $\delta^{13}C$ curve shows a possible poorly defined (3 samples) mid-CIE minimum around a depth of 2167.8m. The first appearance of the *Pseudomonoclimacis latilobus* graptolite fauna was recognised in the upper part of the decreasing limb of the CIE, coeval with bulk rock $\delta^{13}C$ values of 2‰. The gradual decrease of the CIE toward the plateau with values of -2‰ occurs in the next 17 m thick interval. The end of the excursion is coincident with the first appearance of the *Slovinograptus–Formosograptus* graptolite assemblage (Text-fig. 2D; compare Spiridonov *et al.* 2017).

The bulk rock oxygen isotope curve (Text-fig. 3D) is strongly influenced by the changes in dolomite contribution with the additional effect of the different fractionation factor between calcite and dolomite precipitation (Vasconcelos et al. 2005). According to estimations based on paired sample analysis (Text-fig. 13), the oxygen isotope signatures of the dolomite component, after correction for different fractionation factor (Vasconcelos et al. 2005), show heavier (compared to calcite) and more consistent $\delta^{18}O$ values (between -6‰ and -1‰). Oxygen isotope signatures of calcite are significantly lighter (between -18‰ and -6‰) and show presence of the positive correlation with the $\delta^{13}C$ values (Text-fig. 13; compare Samtleben *et al.* 2000).

INTERPRETATION

Eolian induced marine snow in the event prelude interval

The facies anomaly of the Reda Member in the Pasłęk IG-1 borehole section is preceded by earlier, less-pronounced facies changes.

Dolomite silt as eolian dust. Increasing contribution of dolomite silt, just below the main carbonate anomaly (Text-fig. 3H), was noted earlier in the more proximal to palaeo-coastline Mielnik IG-1 borehole section (Kozłowski and Sobień 2012). The silt was interpreted as eolian dust (as in Samtleban *et al.* 2000), based on features (Kozłowski 2015), which are also observed in the case of Pasłęk IG-1, i.e.: a well-sorted silt fraction, a distinct negative skew in diameter (very sharp maximum size limit at 40 μm), the presence of rounded dolomite grains, the lack of dolomite crystal intergrowths, a high mica/quartz ratio and a locally observed peculiar mica-dolomite (quartz depleted) detrital admixture to the calcisiltite facies. The estimations of $\delta^{18}O$ for dolomite (Text-fig. 13; compatible with values obtained from isolated dolomite grains in Kozłowski 2015, fig. 2O) suggest a heavier and more consistent (in relation to calcite) oxygen isotope composition, which is in accordance with dolomite precipitation with the influence of evaporitic waters – residually enriched in ^{18}O (e.g., Pierre *et al.* 1984) in an emergent carbonate platform setting, which was possibly the source of the dolomite dust.

The alternative interpretation of dolomite as having been precipitated inside the aggregates due to the reductive microenvironment does not fit due to the limited size of the dolomite grains, absence of intergrowths, presence of rounded grains, and common sorting with quartz and mica. The eventual derivation of dolomite by intra-basinal transport from the emerged carbonate platform top is excluded by the general opposite direction of detritus derivation for the whole Kociewie Formation, i.e., from the SW located clastic-bearing orogenic wedge (Jaworowski 1971).

In the case of the Pasłęk-IG1 borehole section, the dolomite silt admixture is additionally coeval with red-coloured fine clay laminae and the pink-violet hue of the carbonate facies at the event maximum. Enrichment of pyrite framboids within the red laminae is interpreted as resulting from pulses of iron-bearing dust supplied to the sea surface (dust storms or dust wet deposition), where the long-term suspending finest fraction of eolian material (iron compounds) was concurrently deposited with pyrite, grown with delay in the water column after the iron supply pulse. Enrichment of the red laminae in graptolite fossils may suggest an additional fertilization effect of the dust supply.

Silt aggregates as marine snow. Silt material in the dolomitic mudstones is preferentially incorporated into the aggregates, bonded (and also enveloped) by a clay-organic matrix containing relics of calcified filaments of probably cyanobacterial origin (Text-fig. 4E').

Given the compositional anatomy, overall shape, size, textural arrangement of accumulations and rock-forming abundance, the aggregates are interpreted as marine snow. Modern marine snow (e.g., Alldredge and Gotschalk 1988; Alldredge and Silver 1988; Ransom, *et al.* 1998) occurs as sediment-forming flattened organomineralic aggregates up to several millimetres in size. The detrital material incorporated into aggregates is clay to silt-sized, very often derived as eolian dust. The marine snow particles are held together by organic-rich mucous and phytoplankton filaments in a relatively loose agglomeration; hence the particles have a tendency to be flattened by compaction. The aggregates often join together with partial coalescence. The marine snow particles are often formed in association with phytoplankton blooms, hence have a tendency to occur as horizontal accumulations in the form of horizontal laminae (Grimm, *et al.* 1997).

Iron replacing by active acquisition as exclusive marine snow attribute. It is proposed here, that the observed enrichment of iron around the aggregate ('pyrite halo'), previously described as a feature of Jurassic marine snow (Macquaker *et al.* 2010), can be an important diagnostic feature of the marine snow formed by cyanobacteria.

The substantial part of marine snow in recent oceans is formed by pelagic cyanobacteria (Lampitt *et al.* 1993), especially in the case of eutrophic conditions (Kaltenböck and Herndl 1992). The pelagic diazotrophic cyanobacteria *Trichodesmium* [of Ediacaran origin according to molecular clock predictions (Sánchez-Baracaldo 2015)] actively traps detrital grains for iron acquisition (as a nutrient needed for active nitrogen fixation) and replaces iron from the mineral aggregate toward the external, living part of the floc (Rubin *et al.* 2011). Such a mechanism would result in the formation of a 'pyrite halo' around the cyanobacterial marine snow floc in contrast with pelagic faecal pellets, which are preferentially pyritized inside. The observed partial calcification of the filaments inside the aggregates also matches with the *Trichodesmium* (group) origin,

because it was recently experimentally demonstrated that *Trichodesmium* shows a high potential for carbonate precipitation, especially in bloom conditions (Kranz *et al.* 2010). Moreover, recent *Trichodesmium* blooms are often triggered by iron-bearing eolian dust (Capone *et al.* 1998; Rubin *et al.* 2011) and are associated with water-column stratification. Eolian dust supply can strongly enhance vertical marine carbon export by causing coeval surface water fertilization and by the ballasting effect of lithogenic, eolian material (van der Jagt *et al.* 2018). The enhanced vertical carbon flux caused by eolian fertilization, has the high potential for the formation of bottom anoxic or euxinic conditions.

Development of euxinic conditions

The occurrence of pyrite in the studied rocks, entirely in the form of non-coalescent framboids, points to syngenetic to early diagenetic pyrite formation (Wilkin and Barnes 1997). The pyritization pattern in the studied section is strictly related with facies-mineralogical changes (Text-fig. 3 E *vs*. B+H; Table 1), repeating the scenario noted earlier in the periplatform setting (Kozłowski 2015).

In the event prelude interval, the appearance of eolian-derived detritus and marine snow parallels the gradual evolution of the pyrite framboid population toward the lowermost median, mean and maximum sizes, coupled with low standard deviation and low skewness (A1–A2 in Table 1; Text-fig. 12). The size characteristics and strong domination (>90%) of tiny pyrite framboids (below 5 μm in diameter) suggest pyrite formation in the sulfidic water column (Wilkin *et al.* 1996). Such an indication is confirmed by the absolute lack of overgrown and coalescent framboids and lack of framboids larger than 10 μm (Wignall and Newton 1998) in the A1 sub-suite. The single grains larger than 10 μm in the sub-suite A2 are regarded as an effect of short-lived oxic pulses, which occurred e.g. in the effect of the density current episodes (see the Ps1146s low/up samples in the Table 1 – representing the lower and upper part of the single bed of density current origin). The A1–A2 framboid sub-suites, interpreted as indicating euxinic (A1) or temporary euxinic (A2) conditions, appear a few meters below and occur continuously across the Reda Member carbonate anomaly, with only single point regressions probably caused by density current events (Text-fig. 3E; Table 1).

Below the event interval, less consistent statistical parameters of framboids (B suite) are interpreted as recording lower dysoxic conditions, with similar higher-oxic episodes associated with density currents (as sample Ps1196g – representing facies R). Above the laminated calcisiltite complex, the occurrence of distinctly coarser and often coalescent framboids (C–D suites) points to gradual environmental evolution toward upper dysoxic conditions.

Sedimentary processes and depositional environments of the Reda Member

The apogee of the studied event in the pelagic setting of the Baltic-Podolian Basin is recorded by the unusual mass appearance of carbonate precipitates. The first manifestation of a carbonate saturation rise in the event prelude interval is recorded as an initially gradual and later rapid increase of carbonate incrustation formed around marine snow flakes. Immediately above, the Reda Member contains the massive dominance of calcite crystals, which have been described earlier as 'sparoids' (Kozłowski 2015) and interpreted as carbonate precipitates formed in the water-column (whiting-related endogenic epipelagic suspensoids).

Sparoids as carbonate suspensoids. Recent carbonate suspensoids, similar in shape and maximum size (up to 50 μm), are widely observed in hard water, freshwater environments, where they are formed with the participation of picoplankton photosynthetic activity (Dittrich *et al.* 2004; Dittrich and Obst 2004; Thompson *et al.* 1997). The cyanobacterial origin of suspensoids is evidenced by the entombed cells of picocyanobacteria often preserved as curved holes in the crystal interior or as attached cells (Bosak *et al.* 2004; Chafetz 2013; Dittrich and Obst 2004; Greenfield 1963; Tourney and Ngwenya 2009).

A similar origin of the filaments within the Reda Member sparoids is best evidenced in primary cloudy calcite crystals, by the overgrowth of cloudy anhedral sparoid centres by limpid calcite up to an euhedral shape (Text-fig. 6F), which is interpreted as nucleation around actively photosynthetic cells, subsequently entombed inside by further spontaneous crystal growth (compare Morse *et al.* 2003; Yates and Robbins 1998). These features suggest the formation of the primary cloudy sparoids in the surface photic layer and eventual further growth continuation occurring during suspension and sinking. It is important to note that the surface algal scum forming in bloom conditions could allow for the prolonged suspension and growth of calcite crystals in a surface related environment, as well the formation of calcite incrustations on flocs (e.g. Taylor *et al.* 2004).

The unstained external lattices, observed around

part of the cloudy sparoids were earlier described (Kozlowski 2015) as skeletal dolomite rims and interpreted as having been formed by internal calcification of dedolomite, derived as eolian material from the emergent carbonate platform realm. However, such an origin should cause dispersal distribution of such types of grain and their abundant occurrence in the detrital laminae also as non-calcified skeletal crystals. Current observations reveal a non-dispersal, locally concentrated occurrence of grains with unstained lattice, observed as e.g., an exclusive type of grain in individual aggregates (e.g., Text-fig. 7C) or laminae. Moreover, the grains are "colonised" by microbial filaments only from the inside, whereas their surface shows no signs of cloudy calcite overgrowth (compare such overgrowing of regular detrital dolomite in Text-fig. 6E). Also the detrital laminae contain only very rare, single and collapsed skeletal dolomite rims (which sustains the general presence of some accessorial admixture of dedolomite in the detrital grains population).

The alternative interpretation is that the unstained external lattices of the sparoids represents magnesium 'armouring' (Tribble and Mackenzie 1998) formed during sinking into the stratified water column. The dominant euhedral rhombohedral shapes, as well as the large crystal dimensions indicate a low content of magnesium (Folk 1974) in the near-surface water column, where the sparoids were probably formed. However, the 'armouring' would occur during sinking towards the bottom – into the sulfate reduction zone, where sulfate depletion causes magnesium release from the $MgSO_4^0$ ion pairs, resulting in enhanced magnesium ion activity. Alternatively, the vertical Mg-ion activity gradient would result of a salinity gradient in the stratified water column. The 'magnesium armouring' of mature sparoids suggest that there were unfavourable conditions for the spontaneous growth of 'sparoids' below the sulfate reduction zone.

In this context, the primary limpid sparoids in form of subhedral crystals and coatings are interpreted as being formed also in the surface layer but probably without the strictly photosynthesis-related conditions. The spheroids and ovoid coatings around mineral grains (mainly ?eolian dolomite) as well as spherulites around tiny organic centres, are interpreted as spontaneous calcite growth in supersaturation conditions, occurring in suspension or inside the mucus-organic matter flocs of algal scum.

Sparoid marine snow. In contrast to the earlier described Mielnik IG-1 borehole section (Kozłowski 2015), representing a more proximal (periplatform) part of the basin and containing abundant individual sparoids (Text-fig. 1, no. 14), the sparoids in the Pasłęk IG-1 borehole section occur mainly in the form of various clusters bonded by organic matter – 'flocs' or by anhedral calcite – 'flakes' interpreted here as the marine snow. Aggregates similar to marine snow are often observed also in the case of recent carbonate suspensoids (Braissant *et al.* 2003; Tourney and Ngwenya 2009), which form crystal chains (Freytet and Verrecchia 1993), microstromatolites and spheroids (Buczynski and Chafetz 1991), random clusters and rafts (Taylor *et al.* 2004).

The eventual authigenic formation of such agglomerations on the seafloor is unlikely, due to the strongly limited incorporation of terrigenous grains and absence of pyrite framboids (both of these occur abundantly outside the aggregates), which point to sparoid agglomeration above the pyrite formation zone. Moreover, the aggregates observed in the Pasłęk IG-1 borehole section (e.g., Text-fig. 7) lack palisade encrustations or randomly oriented elongated crystals typical of seafloor crystal fans (e.g., Saitoh *et al.* 2015; see also fig. 7C in Kozłowski and Sobień 2012). The eventual early diagenetic, authigenic calcite precipitation in porous sediment with pyrite replacement by displaced growth is also unlikely due to: (1) the well preserved grain-supported textural arrangement of the primary sparoids (in exceptional cases – sparoid chains and encirclements); (2) the incorporation of detrital (?eolian dust) components not displaced by crystal growth; (3) the parallel occurrence (or internal transition) of the non-calcified 'flocs'.

Direct evidence that at least part of the sparoid aggregates represents unmodified marine snow particles are the soft deformed flocs and long sparoid chains (Text-figs 7D, 8B, 10D). These aggregates are interpreted herein, respectively, as stringers (Eisma 1986), i.e., comet-shaped elongate aggregates; and sheet-like biofilm flocs, both of which are the typical forms of recent marine snow (Alldredge and Gotschalk 1988; Berhane *et al.* 1997; Riebesell 1991; Stachowitsch *et al.* 1990). The co-occurring 'sparoid encirclements' (Text-figs 9E, 10D) are formed around loose individual detrital grains (quartz, dolomite), with relics of filaments on their etched-like surface, interpreted as related to active nutrient (?iron) acquisition by bacteria. The attached cells were probably nucleation sites for the calcite crystals, with their growth induced by photosynthesis. The 'encirclements' interpreted as being formed in the upper (photic) water column are regarded as the initial stage of the larger sparoid aggregate formation (compare Taylor *et al.* 2004).

Accumulations of aggregates in the form of horizontal bands (Text-fig. 9A) are comparable to the pelleted texture of quasi-laminae described by Macquaker *et al.* (2010) and Dela Pierre *et al.* (2014) interpreted as single-event units (microbeds) that originate from algal-bloom related massive settling of marine snow.

On the bottom, thicker accumulations of recent marine snow form agglomerations of multi-species clumps, where individual flocs could still be recognised (Stachowitsch *et al.* 1990). In the studied case part of the thick laminae has locally preserved a graded stack (Text-fig. 10A) or resembles the chaotic accumulation (Text-fig. 10B–C) of individual, still recognizable flocs. The chaotic texture of facies Db and some laminae also preserves the original chaotic arrangement of densely tangled sparoid chains and encirclements (Text-fig. 10D). The composition of such horizons may be interpreted as representative for the composition of the original (non-reworked) suspended sediment, largely composed of marine snow aggregates, with the admixture of individual grains.

Pyrite, interpreted as forming in the water column, is extremely depleted inside the 'sparoid' aggregates and their accumulations. This is interpreted as being related: (1) to the formation of aggregates above the sulfidic zone (internal depletion); (2) to temporal events of very fast sparoid precipitation and massive settling, occurring in the context of constant clay-pyrite sedimentation (inter-aggregate depletion); and possibly (3) to hydraulic sorting on the bottom surface (see below). The overall volumetrically (at least double) pyrite depletion in the whole 'sparoid' interval is interpreted as being caused by a (*ca.* double) increase of the relative rate of sedimentation caused by the mass extra-addition of 'sparoid' calcite.

Textural arrangement by benthic flocculent layer. The settling of sparoids mostly as aggregates should result in a pelleted texture, however this does not explain the significant lateral changes in thickness and the wavy (pinch and swell) geometry of laminae composed of individual sparoid accumulations (Text-fig. 8A). Compared to the spectrum of texture variations in recent marine laminated sediments (Schimmelmann *et al.* 2016), the observed specific texture is very similar to the textural arrangement of the abyssal coccolith ooze of the Black Sea, which is strongly modified by additional hydraulic sorting and early diagenetic alternation by the 'benthic flocculent layer' (Pilskaln and Pike 2001). The 'fluff layer' has been recognised in several places in the recent ocean, where it is formed due to the massive deposition of phytodetritus (marine snow) in consequence of massive phytoplankton blooms (Beaulieu 2002). In the case of the Black Sea, the 'fluff layer' is a 2 cm thick layer of loose gelatinous consistency underlain by 2 cm of thick unconsolidated sediment. Hydraulic sorting in the layer favours for the separation of carbonate, lithogenic, pyrite and organic material. The concentrated sinking of the grains in the gelatine layer results in the compositionally well separated laminae of pure carbonate laminae with a 'pinch-and-swell' geometry (Pilskaln and Pike 2001).

The laminated calcisiltite facies show certain features that may indicate the presence of such a layer also in the studied case. The common undulate bases of laminae (Text-figs 8A, 9A) suggest deposition on an unstable water-sediment interface with inverted density. The load structures (Text-fig. 8B) are associated with internal normal grading (see also Text-fig. 8C, D), which could be the result of hydraulic sorting in a fluff layer. This is in line with the generally high degree of carbonate *vs*. lithogenic + pyrite grains separation in the laminated facies. Parts of the thick laminae (Text-fig. 10B, C) are composed of loose soft-deformed flocs dipped in the organic-clay matrix, preserving the textural arrangement expected for original fluff-like accumulation.

Record of density currents. The Reda Member occurs within the Kociewie Formation, which contains numerous beds of siltstones interpreted as being formed by turbidity currents (Jaworowski 1971; Jaworowski 2000). The siltstone contribution distinctly increases towards the base of the Reda Member; inside the member, however, the record of redeposition is surprisingly sparse and represented by single intercalations of massive to cross-laminated calcisiltites occurring in two microfacies varieties (facies Da and Db).

In the first variety (Da), the bulk composition of a single bed seems to be compositionally equal with the virtually averaged bulk material of the Reda facies content (A, B, C, M); hence, it is interpreted as bottom material reworked by the traction turbidity current (turbidite). The facies contain individual sparoids, 'rigid' calcite flakes, as well as sparoid agglomerations (flocs, chains, encirclements), which confirms the complex pre-diagenetic composition of the original sediment, corresponding to that recognised in the laminated facies record.

The second variety (Db) of pure calcisiltites (graded or cross-laminated) is strongly depleted in lithogenic grains, which are additionally overrepresented by dolomite and mica. Distinct quartz depletion suggests that such detrital material is mainly of eolian origin. The presence of abundant vase-shaped

microfossils (interpreted as tintinnids) is regarded as microzooplankton associated with marine snow (see e.g., Lampitt *et al.* 1993). Similar fossils are very rare and poorly preserved in the laminated facies, which indicates the relatively rapid replacement and deposition of carbonate material in facies Db.

Given the anomalous enrichment in well-preserved organised sparoids (chains, encirclements), eolian related detrital component and specific fossils, variety Db is regarded as having been formed by vertical hyperpycnal flows, generated by the downwelling of a whiting-related surface water plume (surface nepheloid layer). Formation by similar vertical flows is recognized in the case of carbonate platform margins (Wilson and Roberts 1992) and as a consequence of the deposition of fine pyroclastic material on the water surface (Manville and Wilson 2004).

Low efficiencies of organic matter burial and possible methanogenesis traces

The euxinic conditions postulated above and the high organic matter influx to the bottom sediment by its deposition as marine snow contrast with the very low content of OM in the Reda rocks, observed also beside sparoid laminae – where the dilution effect is expected. Moreover, the laminated facies preserves separate red clay laminae (which results in the red hue of the Reda facies), with horizontally occurring oxidized pyrite framboids, which indicates that the OM content during diagenesis was not sufficient for the retention of reductive conditions around concentrated oxide compounds in the sediment.

Middelburg *et al.* 1993 postulates that the OM burial efficiencies are similar in oxic and anoxic sedimentary conditions and mostly depends on the bulk sediment accumulation rate i.e. time of exposure of the OM to bottom surface processes. For example, despite the euxinic conditions, the OM burial efficiency in the Black Sea is similar to that of oxygenated environments in similar settings (Calvert *et al.* 1991; Calvert and Karlin 1998). The pronounced decrease of the OM content observed across the upper few centimetres of the bottom sediments of the Black Sea (Calvert *et al.* 1991, fig. 2) is related to the hydraulic sorting of the OM in the fluff layer, which reduces potential OM incorporation into the final sediment. The prolonged residence of the OM particles in the bottom-related flocculent layer favours its intensive anoxygenic degradation by methanogenesis and sulfate reduction (Jannasch 1991; Pilskaln and Pike 2001), hence strongly reducing the potential OM burial rate. In a similar way, the observed final OM-depletion in the Reda facies is interpreted as having been caused by intense anaerobic OM decomposition operating for instance inside the benthic flocculent layer.

The CO_2, which is the by-product of methanogenesis, is expected to cause acidification leading to carbonate dissolution (the "methanogenic carbonates" paradoxically are formed as a result of methanotrophy – not methanogenesis). The local traces of partial dissolution along sub-vertical pore system paths (facies Db, single thick laminae in facies A–B; Text-fig. 11) are interpreted as possible effects of vertical migration of dissolved methanogenic CO_2 along the primary porosity. Because the structures concern individual layers or laminae formed by rapid sedimentation (facies Db), they are interpreted as forming inside the surface sediment layer, probably immediately after deposition with burial of the methanogenic 'benthic flocculent layer'. The laminated facies shows in general only rare signs of similar dissolution, or fluid migration, which is in line with the localization of OM-degradation (methanogenesis) mainly in the surface sediment fluff layer.

The dissolution related porosity is followed by precipitation of the secondary, anhedral, neomorphic dolomite cement (Text-fig. 11, see also: Text-fig. 6C, H). The cement is regarded as possibly representing early diagenetic dolomite formation in a methanogenic marine environment (Irwin *et al.* 1977; Meister *et al.* 2011 and references therein). Marine bacterial methanogenesis by CO_2 reduction causes strong kinetic fractionation (Alperin *et al.* 1992; Botz *et al.*; 1996; Claypool and Kaplan 1974), hence the dissolved CO_2 (returned to the DIC reservoir), formed as a by-product of methanogenesis, is strongly enriched in ^{13}C (Meister *et al.* 2019). However, the samples containing anhedral dolomite cement do not show significant or consistent $\delta^{13}C$ enrichment, which would have confirmed such an origin; however, the relatively low cement contribution and the generally heavy $\delta^{13}C$ signatures of the host calcisiltite may strongly suppress such a signature. The isotopic identification of the component is also hindered by the co-occurrence of detrital dolomite with relatively low $\delta^{13}C$ values.

DISCUSSION

Origin of the carbon isotope record of the Reda Member carbonates

One of the widely reported features of the early Palaeozoic CIEs is the declining amplitude of the

carbon isotope anomaly towards offshore areas (e.g. LaPorte *et al.* 2009; Loydell 2007; Munnecke *et al.* 2003; Noble *et al.* 2012). In this context, the few studied pelagic sections, representing the deep-water Ockerkalk facies of Sardinia and the Carnic Alps (Jeppsson *et al.* 2012) do not record the mid-Ludfordian CIE in the carbonate component. On the other hand, Underwood *et al.* (1997) as well as Melchin and Holmden (2006a) recognised that the Hirnantian–Llandovery CIEs are recorded even in the undoubtedly oceanic succession of the Dob's Linn section (Scotland), however only in the surface-related organic-matter carrier (see also Noble *et al.* 2012).

Because the carbonate components are commonly formed in a seafloor (benthic) related environment, the offshore declining amplitude of the CIE in carbonates probably reveals a vertical, depth-related ^{13}C decrease of the Dissolved Inorganic Carbon (DIC) reservoir. The very high amplitude of the mid-Ludfordian CIE in the pelagic, deep-water carbonates of the Reda Member (identical with the carbonate record of the littoral part of the basin), seems surprising and has two possible explanations.

The first possibility is the authigenic, early diagenetic origin of the high $\delta^{13}C$ values, detached from the shallow water CIE record. In this scenario the Reda Member carbonates would be formed by benthic authigenic precipitation in a methanogenic environment (seafloor, 'fluff layer' or shallow burial), with a dominant contribution of the DIC created *in situ* by dissolution of ^{13}C-enriched CO_2, originating as a by-product of methanogenesis. Such an interpretation is problematic, firstly because of the wide and varied spectrum of textures and grains described in this paper, which refer to the endogenic-sedimentary nature of the sparoids, with a parallel lack of textures typical of seafloor precipitation. The hypothetical authigenic sparoid formation in a methanogenic environment is also implausible for a few general reasons.

The ^{13}C-enriched methanogenic carbonates are formed in Mg-rich (marine related) but sulfate depleted (below the sulfate reduction zone) conditions, which results in the high activity of the Mg^{2+} ion and predominant dolomite mineralogy (Meister *et al.* 2011), whereas the Reda Member is preferentially composed of calcite. Moreover, methanogenic carbonates need spatial detachment between the low-pH methanogenic sub-environment and alkaline conditions needed for carbonate formation, hence in general they are associated with a burial diagenetic environment (Bojanowski 2014; Kelts and McKenzie 1982), and not with the sediment-water interface (fluff layer). CO_2 acidification needs to be neutralized by a rich source of alkalinity, such as weathering of the deeper methanogenic sediment section (Wallmann *et al.* 2008), rich in reactive silicate minerals. Hence, formation of methanogenic dolomites would be caused by the prolonged sedimentation of OM-rich anoxic sediments, but not short-lived anoxic event conditions. The efficient *in situ* alkalinity generation by silicate weathering should additionally result in the formation of residual authigenic minerals (kaolinite, silica), which are not observed in the Reda Member nor in the underlying rocks.

The sub-vertical traces of calcite dissolution, succeeded by the formation of scarce dolomite cement in secondary porosity, observed locally in microfacies Db, are interpreted as possible traces of methanogenesis related to the processes discussed above (with alkalinity obtained from calcite dissolution). However, the samples containing dolomite cement show similar $\delta^{13}C$ values to the adjacent cement-free samples, which indicates that the potential contribution of *in situ* generated methanogenic $^{13}CO_2$ was subordinate (and concurrent) in relation to the pronounced, positive $\delta^{13}C$ values in the calcite background. The association of the structures with the rapidly deposited sediments of microfacies Db is in line with the surface 'fluff layer' as a focal point of methanogenic OM remineralization.

The second (preferred) explanation of the pronounced CIE in the basin axis is in line with the endogenic formation of calcite (see Kozlowski 2015). In this variant, sparoids (in similarity to OM), record high $\delta^{13}C$ values of DIC in the epipelagic layer. An identical record of the CIE in both epipelagic and shallow-water, benthic-littoral carbonates implies the widespread lateral unification of the sea-surface DIC reservoir. In contrast, the benthic, offshore (sub-litoral) carbonates in the same basin, record (as reviewed in Kozłowski and Sobień 2012) the depth-related CIE-decline of the benthic-bioclastic component, with a minimum CIE amplitude at the carbonate platform edge (e.g. +5.02‰ in the Milaičiai-103 section; Spiridonov *et al.* 2017).

It has been proposed (Kozłowski 2015) that the strong ^{13}C enrichment of the epipelagic layer in epeiric basins during the Lau event would be formed in result of concurrent: (1) residual effect of the effective biological pump due to dust-fertilized surface algal blooms; (2) preferential $^{12}CO_2$ degassing due to evaporation and carbonate precipitation in carbonate platform tops (and/or epipelagic zone); and (3) eolian-driven (high N/P ratio) upper water-column methanogenesis (Kozłowski and Sobień 2012; *see also* Beversdorf *et al.* 2010; Carini *et al.* 2014; Karl *et al.* 2008), causing

residual net ^{13}C-enrichment of DIC, due to the loss of the ^{12}C-enriched CH_4 to the atmosphere.

The eventual contribution of methanogenic $^{13}CO_2$ derived from concurrent methanogenic decomposition of OM operating in the benthic flocculent layer, is rather improbable, due to the expected parallel oxidation of the ^{12}C-enriched coproduced methane in the water column, without any net isotopic effect. The recently reported euxinic condition in the Baltic-Podolian Basin (Bowman *et al.* 2019; Kozłowski 2015; and this paper) additionally point to basin stratification during the event. The limited mixing between the surface and deep water DIC reservoirs would have also strongly amplified the depth-related $\delta^{13}C$ gradient formed by the sea-surface related processes.

The local temporal deep-water ^{12}C sequestration, as well as loss of local sea surface-related ^{12}C as CO_2 and CH_4 (Kozłowski 2015), operating in such stratified epicontinental basins as the Baltic-Podolian Basin, are an alternative for the initial explanation of the early Palaeozoic CIEs by enhanced global burial of organic carbon in the deep ocean (Brenchley *et al.* 1994; Kump and Arthur 1999; Wenzel and Joachimski 1996). The global burial model is not supported by OM enrichment in the deep shelf and the oceanic rock record (Farkaš *et al.* 2016; Melchin and Holmden 2006a; Munnecke *et al.* 2010; Munnecke *et al.* 2003; Noble *et al.* 2012). Moreover, global carbon sequestration in sediments does not fit the rapid decline of the CIE toward the pre-event plateau level and laterally various CIE amplitudes. In this context, anoxygenic OM decomposition combined with local strong basin stratification solves the problem of the lack of organic carbon enrichment in the mid-Ludfordian sedimentary rocks (see Munnecke *et al.* 2003), with ^{12}C temporary sequestered as DIC in the deep-water reservoir in the stratified basins, or exported to the atmosphere in the form of CO_2 and methane. The later fate of such exported ^{12}C-enriched carbon (after oxidation) would be its recurrent solution in the ocean; however this would be preferentially localised in cold-water areas with a negative ocean-atmosphere pCO_2 gradient (e.g. high latitude areas where Silurian CIE's are not observed).

It is important to note that the short-lived stratification of the epicontinental seas did not cause the nutrient depletion negative feedback, particularly in the abundance of eolian dust fertilization, which led to high N/P conditions, which are favourable for sea-surface methanogenesis (Beversdorf *et al.* 2010; Carini *et al.* 2014; Karl *et al.* 2008).

Another (local) factor influencing (negatively) the bulk-rock CIE amplitude in the bulk-rock record in the studied basin is the land-derived detrital (older) dolomite, with flat-low $\delta^{13}C$ values across the CIE (Kozłowski 2015). It may be expected that this component should be winnowed from the proximal high-energetic littoral zone (with its minor influence on the high CIE amplitude) to the periplatform setting, where its preferential deposition maximum, concurrent with low $\delta^{13}C$ values of the deeper, benthic, sub-littoral carbonate component, would cause substantial suppressing of the CIE amplitude of the carbonate platform margin facies (+5.02‰ in the Milaičiai-103 borehole section – Spiridonov *et al.* 2017; +6.74‰ in the Mielnik IG-1 borehole section – Kozłowski and Sobień 2012). Assuming the eolian origin of the dolomite component, its contribution should decrease toward the basin axis, which coupled with the diminishing of the benthic carbonate component and the overwhelming domination of sparoid calcite, recording a clear sea-surface related high CIE amplitude.

The problem of sparoids: is endogenic carbonate precipitation present in recent seawater?

Endogenic carbonates are commonly observed in recent fresh-, hard- water reservoirs of lacustrine and karst environments. In contrast, carbonate suspensoids are not recognised as typical and widespread components of the marine carbonate rock record and in recent marine deposits. Despite the fact that the recent surface ocean is highly supersaturated with respect to calcite (Ω = 4.8) and aragonite (Ω = 3.2; e.g., Ridgwell and Zeebe 2005), spontaneous 'chemogenic' precipitation directly from seawater is not observed. Nucleation and further crystal growth of carbonate minerals is strongly limited by the low activity of the carbonate ion, cation hydratation, formation of highly soluble ion pairs (e.g., $Na_2CO_3^0$), the presence of foreign ions (e.g., Mg^{2+}, SO_4^{2-}) and organic compound coatings around potential nucleation sites (for review see e.g., Nielsen *et al.* 2016; Troy *et al.* 1997; Wright and Oren 2005 and references therein). Inhibitor effects result in each marine carbonate precipitation process in the recent ocean needing an additional local increase of carbonate saturation or biomediation (e.g. Morita 1980; Wright and Oren 2005; Yates and Robbins 2001 and references therein). Bioinduced precipitation may occur as the result of the rapid sink of CO_2 in photosynthesis (e.g. Yates and Robbins 1998; Thompson 2000) and may be present in the surface ocean, especially due to massive picoplankton blooms (e.g. Long *et al.* 2017).

In this context, the origin of marine 'whitings' (drifting clouds of milky carbonate mud suspended in water) is a topic of long-lived discussion, with the presentation of strong arguments both for 'direct chemogenic or bioinduced precipitation' (Morse and He 1993; Robbins and Blackwelder 1992; Robbins *et al.* 1997; Thompson *et al.* 1997; Wells and Illing 1964) or the 'resuspension' nature of the phenomenon (Broecker *et al.* 2000; Morse *et al.* 2003; Morse *et al.* 1984; see discussion in Shinn *et al.* 1989). Recent whitings are observed mostly in shallow-littoral top-bank water masses (Florida, Bahama), where the resuspension mechanism may be important or dominant. However, in the case of the Persian Gulf, whitings occur in the deeper ramp setting (Wells and Illing 1964) and are related to combined enhanced carbonate saturation (due to evaporation) and massive carbon dioxide consumption by phytoplankton during algal (diatom) blooms (Wells and Illing 1964), which in turn may be induced by iron-bearing eolian dust (see Kendall and Alsharhan 2011; Nezlin *et al.* 2010). Such a case shows that the tropical, eolian fertilized, mediterranean (foreland basin) seas, with strong evaporation and high carbonate saturation are favourable for bio-induced carbonate suspensoid formation in the water column.

Less concentrated, but widespread bioinduced microbial carbonate precipitation occurs also in the proper pelagic realm. Recently, Heldal *et al.* (2012) noted heterogeneous calcite precipitates with shapes characteristic of bacterial precipitation, as well as surface-water formed 'calcite rafts' (!) in a few localities in the Mediterranean Sea, the Norwegian Sea and the North Atlantic Ocean. Such findings suggest that carbonate suspensoids may be widespread, but the mass abundance of coccolithophores and foraminifera in the recent ocean, causes extreme dilution of potential non-skeletal, epipelagic carbonate components in the sediment. Moreover, the effective discharge of carbonate saturation by bio-skeletal grain production in recent pelagic environments, effectively stabilises carbonate saturation at a relatively low level (Ridgwell 2005), which is not conducive for competitive microbially bioinduced precipitation. Thus, such precipitation more commonly appears in restricted marine environments (see below), where competitive skeletal calcifiers are absent (see e.g., Davis *et al.* 1995; Dix 2001; Glenn *et al.* 1995).

The carbonate suspensoids appear most abundantly in semi-isolated marine anoxic stratified basins (Degens and Stoffers 1976). In the recent anoxic fjords and marine lakes (filled with marine water), the effects of the absence (or limited presence) of skeletal calcifiers concur with the effective production of additional alkalinity by anaerobic degradation of OM, coupled with sulfate reduction and pyrite formation (Black 1933; Kempe 1990; Kempe and Kaźmierczak 1994; Lalou 1957).

In the Framvaren Fjord (Noway), the excess of alkalinity produced by sulfate reduction (Yao and Millero 1995), coupled with diminishing of sulfate inhibition (Nielsen *et al.* 2016), results in chemogenic (possibly bioinduced) endogenic carbonates (Anderson *et al.* 1987; Müller 2001). Calcite crystals identified in both sediment trap and bottom sediments are up to 100 μm in size and resemble the suspensoids noted from modern lacustrine environments.

Also in the case of the karstic Mediterranean marine lakes (infilled by marine water), the alkalinity enhanced by bottom anoxic conditions results in massive surface carbonate precipitation (calcite or aragonite) triggered by nanophytoplankton [(Etoliko Lagoon – (Koutsodendris *et al.* 2015); Lake Butrint – (Ariztegui *et al.* 2010); Mljet Island lakes – (Sondi and Juračić 2010); Zmajewo Oko – (Bakran-Petricioli *et al.* 1998)].

In the case of the deep Black Sea basin, alkalinity generated by sulfate reduction causes a 1.6 times higher level in comparison with the surface of the global ocean (Goyet *et al.* 1991), however it is consumed today mainly by coccolithophores [recent euxinic Black Sea sediments contain also some admixture of carbonate suspensoids ("Weizenkorn" of Müller and Blaschke 1969]. However, subfossil Black Sea sediments, dated at 11,400 and 8,400 years BP (Major *et al.* 2002), which formed during glacial isolation and the absence of coccolithophore plankton, are entirely composed of carbonate suspensoids arranged in laminated carbonate muds, very similar to the Reda Member facies. The subfossil carbonate layers in the Black Sea are composed of euhedral, silt-sized calcite crystals (Stoffers and Müller 1978). They are interpreted as being precipitated in the water column from high phytoplankton activity (Bahr *et al.* 2005). It is important to note, that the carbonates show also a distinct, positive carbon and oxygen isotope shift (fig. 5 in Bahr *et al.* 2005), in this case, however, unrelated to the global carbon cycle or event. This shows the high autogenous potential for epipelagic massive carbonate precipitation in the formation of a detached (or eventually globally synchronised) CIE.

A similar massive pelagic carbonate precipitation is also recognised in the post-glacial marine ingression in the Sea of Marmara (Reichel and Halbach 2007). This marine (moreover calcite) scenario is attributed to the post-glacial transition from lacustrine

to marine conditions and explained by the contact of anoxic deep lacustrine (re-connected Black Sea) water with surface oxic marine Mediterranean Sea water.

Silurian ocean and anoxic events: more favourable conditions for sparoid formation?

In the modern ocean, the circumstances presented above, favourable for endogenic carbonate formation, are met in specific, often restricted environments. However the different ion-composition, biology, as well as different oxic-state, of the early Palaeozoic oceans, would allow for the more common formation of epipelagic, endogenic calcite.

The high concentration of magnesium and sulfate ions in recent seawater inhibits calcite growth and causes the small maximum dimensions of calcite crystals (Berner 1975; De Groot and Duyvis 1966; Folk 1974; Mucci and Morse 1983; Tribble and Mackenzie 1998; Wollast *et al.* 1980). In contrast, the Silurian ocean, containing low concentrations of magnesium and sulfates (Arvidson *et al.* 2006; Lowenstein *et al.* 2003; Lowenstein *et al.* 2001), could have promoted inorganic/bioinduced carbonate precipitation (Arvidson *et al.* 2014; Berner and Mackenzie 2011; Riding 1982) and could have allowed for the more common formation of calcite suspensoids. Lee and Morse (2010) have experimentally shown that in reconstructed ambient "Cretaceous" seawater (similar in composition to Silurian seawater), common spontaneous inorganic carbonate nucleation and precipitation may have been possible. Berner and Mackenzie (2011) calculated a large difference between the burial flux and the preservation flux of sedimentary carbonates in Palaeozoic times and postulated an original high amount of Palaeozoic deep-sea carbonates (subsequently destroyed by subduction), probably non-skeletal in nature. Concurrently, pelagic skeletal carbonate production, competitive with bioinduced/inorganic endogenic carbonate formation, was probably very limited in the early Palaeozoic 'Neritian' ocean mode (Zeebe and Westbroek 2003). The short event of 'Neritian' conditions at the K/T boundary (large calcified nanoplankton crisis) results in the appearance of 'non-biogenic' carbonate grains in the pelagic record of the Bidart section, reported by Minoletti *et al.* (2005). A similar Cretaceous 'micarbs' component, recorded in pelagic limestones, at least in part may represent fossil carbonate suspensoids (Beltran *et al.* 2009).

Favourable global circumstances for endogenic carbonate formation would have been additionally intensified during Silurian anoxic events. During the Lau event, globally widespread (but possibly detached) carbonate hipersaturation conditions could have been achieved by concurrent (see Kozłowski 2015 and references therein): (1) intense carbonate dissolution in emerged carbonate platform areas, (2) deep ocean dissolution of eolian carbonate dust, (3) intense sink of CO_2 by phytoplankton blooms driven by eolian dust fertilization, (4) massive pyrite formation (sulfate-bicarbonate charge transfer), and (5) depletions in calcite precipitation inhibitors (sulfate reduction; dolomitization-related magnesium sink).

Most of the previously noted, possibly pelagic carbonate precipitates in the rock record suggest their preferential formation in stratified anoxic basins, where additional alkalinity would be generated. The closest case of the reported mass occurrence of fossil calcite suspensoids is in the upper Permian (Zechstein) Marl Slate, where calcite rhombohedra are interpreted as suspensoids co-occurring with dolomite silt in the anoxic-euxinic facies (Sweeney *et al.* 1987; unfortunately, the grains and facies are not illustrated). Epipelagic, microbially-induced carbonate precipitation in the latest Permian anoxic seas was recently reported by Wu *et al.* (2014; 2016). The described forms of calcite bear morphological similarity to the sparoid chains and are interpreted as fossil casts formed by the planktic cyanobacterium *Microcystis* that commonly forms blooms in modern lakes, rivers, and reservoirs. Massive accumulation of calcite 'microspheroids' produced by cyanobacteria in the water column of the anoxic Cenomanian–Turonian basin (OAE2) is also postulated in the case of the Indidura Formation in Sierra de Parras in Mexico (Duque-Botero and Florentin 2008).

The above presented cases indicate that the Baltic-Podolian sea in the time of the Lau event had exceptionally favourable conditions for endogenic carbonate formation in the epipelagic setting. The Silurian sea-water ionic composition (calcite sea), lack of pelagic skeletal carbonate production ('Neritian' ocean) and enhanced carbonate saturation (global Lau event) were superimposed on favourable palaeogeography, comparable with the recent setting of the Persian Gulf whitings [tropical, eolian-fertilized, mediterranean sea (foreland basin), with enhanced evaporation]. Hence, the record of the mid-Ludfordian event in the Baltic-Podolian Basin was probably strongly amplified by local conducive circumstances. The result is that the common interpretation of the Baltic Basin record as representative of the global ocean during the mid-Ludfordian event needs be carried out with greater caution.

CONCLUSIONS

- In the axial part of the Baltic-Podolian Basin, the Lau/kozlowski extinction level is immediately succeeded by the Reda Member, formed of endogenic carbonate suspensoids. The carbonate facies anomaly precisely coincides with the pronounced, globally recognised, mid-Ludfordian CIE.
- The occurrence of sparoid facies in the Pasłęk IG-1 borehole section indicates that the formation of endogenic carbonate during the event was not limited to the spreading of water bodies over the carbonate platform (platform-top to periplatform whitings; Kozłowski 2015), but occurred also in the strictly pelagic realm. As a result, the Reda Member is recognised as probably one of the oldest cases of undoubted (but nontypical) pelagic carbonates in Earth's history.
- The detrital and endogenic (carbonate) grains in the basin axis are preferentially incorporated into rock-forming organic-mineral aggregates, interpreted as marine snow. The common incorporation of dolomite into marine snow is in line with its presence in the upper water column, which supports an earlier postulated, eolian derivation of dolomite from the emerged carbonate platform top (during the mid-Ludfordian lowstand). Periodical accumulations of marine snow were probably caused by phytoplankton blooms induced by eolian fertilization.
- The record of pyrite framboids indicates that euxinic conditions began a few meters below and disappeared with the end of the Reda Member carbonate anomaly. The euxinic event in the entire Baltic-Podolian Basin is thus coincident with the mid-Ludfordian facies-isotope anomaly.
- The specific pinch and swell, varve-like lamination is interpreted to be the result of the hydraulic sorting effect by the 'benthic flocculent layer', whose presence is expected in the high OM flux regime. The presence of such a layer is also expected due to the low TOC of the Reda Member rocks, most probably resulting from anoxygenic (?methanogenic) decomposition of OM inside the 'fluff layer'.
- The CIE in the Pasłęk IG-1 borehole section does not fit in the paradigm of the offshore decline of the CIE magnitude in the carbonate component. The pronounced CIE amplitude in the Reda Member is comparable with that of the the proximal carbonate platform record. It is proposed that the basinward CIE decline is not a function of distance to the shoreline, but depends on the absolute depth of carbonate formation, and in this case the Reda Member sparoids were formed in the epipelagic, surface layer (photic zone) of the basin. Such a model is consistent with the surface related nature of carbon isotope fractionation processes operating during the mid-Ludfordian CIE (OM-formation in phytoplankton blooms, CO_2-kinetic degassing, surface layer methanogenesis).
- The high amplitude of the Mid-Ludfordian CIE in the Baltic-Podolian Basin was probably strongly amplified by the basin stratification, with a high $\delta^{13}C$ gradient between the surface and deep water DIC reservoirs. It is not clear if the processes operated only on a local scale or are part of a global scenario. The very high amplitude noted in the pelagic facies in the axial part of the Baltic-Podolian Basin does not support the simple weathering hypothesis (Kump *et al*. 1999; Melchin and Holmden 2006b) of CIE formation. However, increased weathering would cause a massive supply of nutrients and carbonate dust, indirectly as well as directly (carbonate dissolution) increasing carbonate saturation. The observed CIE record in the studied basin also does not support the "circulation changes model" (Bickert *et al*. 1997) between the shelf and oceanic realm, suggesting rather local stagnation confirmed by the local development of euxinic conditions in the mediterranean semi-isolated basin. The nutrient depletion problem (paradox), which is often regarded as a limiting factor for persistent anoxia in stratified conditions, would be resolved in enhanced eolian fertilization conditions, which would lead to enhanced primary production with a concurrent high N/P nutrient ratio regime, favourable for surface methanogenesis.
- The Reda Member was deposited under the additionally positive influence of a special local palaeogeography (mediterranean sea), in analogy to the recent Persian Gulf. In the Gulf limited circulation with the open ocean; the local presence of emerged carbonate platforms as a source of dust and bicarbonates and enhanced evaporation due to the low latitude situation results in the presence of pelagic whitings. The partial separation of the Baltic-Podolian Basin would result not only in its having a peculiar facies record, but also in amplification of the CIE amplitude.
- The Baltic-Podolian sea, as a typical foreland basin, had characteristic facies (sparoid pelagic carbonates) and characteristic redox conditions (euxinia). The possibility of the formation of ocean-detached positive carbon isotope anomalies in semi-enclosed anoxic basins (Bahr *et al.*

2005; Birgel *et al.* 2015; Giddings and Wallace 2009; Peryt *et al.* 2012) does not explain the synchronicity of the mid-Ludfordian CIE in the shelf successions of other palaeocontinents (Jeppsson *et al.* 2012; Jeppsson *et al.* 2007; Lehnert *et al.* 2007; Loydell and Frýda 2011). Hence, it may be speculated that the mid-Ludfordian CIE/facies event in the Baltic-Podolian sea could have had one or more of a number of global triggers (such as short-lived glaciations, dustiness, sea-level fall, ocean stratification, carbonate hipersaturation, formation of anoxic conditions), but was strongly amplified by local conducive circumstances.

Acknowledgments

This study was supported by the National Science Centre, Poland, NCN Grant No. UMO-2012/05/B/ST10/00571. Grzegorz Widlicki is thanked for the preparation of polished thin sections. Grzegorz Kaproń is thanked for the XRD analyses. My sincere gratitude goes to Maciej Bojanowski and an anonymous reviewer, as well as Chief-Editor Piotr Łuczyński, for their comments significantly improving the manuscript. Special thanks go also to Anna Żylińska for linguistic support and reading of an earlier version of the manuscript.

REFERENCES

Alldredge, A.L. and Gotschalk, C. 1988. In situ settling behavior of marine snow 1. *Limnology and Oceanography*, **33** (3), 339–351.

Alldredge, A.L. and Silver, M.W. 1988. Characteristics, dynamics and significance of marine snow. *Progress in Oceanography*, **20**, 41–82.

Alperin, M.J., Blair, N.E., Albert, D.B., Hoehler, T.M. and Martens, C.S. 1992. Factors that control the stable carbon isotopic composition of methane produced in an anoxic marine sediment. *Glob. Biogeochem. Cycles* **6**, 271–291.

Anderson, L.G., Dyrssen, D. and Skei, J. 1987. Formation of chemogenic calcite in super-anoxic seawater – Framvaren, southern Norway. *Marine Chemistry*, **20** (4), 361–376.

Ariztegui, D., Anselmetti, F.S., Robbiani, J.M., Bernasconi, S.M., Brati, E., Gilli, A. and Lehmann, M.F. 2010. Natural and human-induced environmental change in southern Albania for the last 300 years – Constraints from the Lake Butrint sedimentary record. *Global and Planetary Change*, **71** (3-4), 183–192.

Arvidson, R.S., Mackenzie, F.T. and Berner, R.A. 2014. The sensitivity of the Phanerozoic inorganic carbon system to the onset of pelagic sedimentation. *Aquatic geochemistry*, **20** (2-3), 343–362.

Arvidson, R.S., Mackenzie, F.T. and Guidry, M. 2006. MAGic: A Phanerozoic model for the geochemical cycling of major rock-forming components. *American Journal of Science*, **306** (3), 135–190.

Bahr, A., Lamy, F., Arz, H., Kuhlmann, H. and Wefer, G. 2005. Late glacial to Holocene climate and sedimentation history in the NW Black Sea. *Marine Geology*, **214** (4), 309–322.

Bakran-Petricioli, T., Petricioli, D. and Požar-Domac, A. 1998. Influence of isolation and peculiar ecological properties on biodiversity – an example of marine lake Zmajevo Oko near Rogoznica (Adriatic Sea). *Rapports et proces verbaux des réunions – Commission internationale pour l'exploration scientifique de la mer Méditerranée*, **35** (2), 518–519.

Barrande, J. 1850. Graptolites de Boheme, 74 pp. Bellmann; Prague.

Bassett, M., Kaljo, D. and Teller, L. 1989. The Baltic region. In: Holland, C.H. et al. (Ed.), A global standard for the Silurian System. *Geological Series*, **9**, 158–170.

Beaulieu, S.E. 2002. Accumulation and Fate of Phytodetritus on the Sea Floor. *Oceanography and Marine Biology, An Annual Review*, **40**, 171–232.

Beltran, C., De Rafélis, M., Person, A., Stalport, F. and Renard, M. 2009. Multiproxy approach for determination of nature and origin of carbonate micro-particles so-called "micarb" in pelagic sediments. *Sedimentary Geology*, **213** (1-2), 64–76.

Berhane, I., Sternberg, R.W., Kineke, G.C., Milligan, T. and Kranck, K. 1997. The variability of suspended aggregates on the Amazon Continental Shelf. *Continental Shelf Research*, **17** (3), 267–285.

Berner, R. 1975. The role of magnesium in the crystal growth of calcite and aragonite from sea water. *Geochimica et Cosmochimica Acta*, **39** (4), 489–504.

Berner, R.A. and Mackenzie, F.T. 2011. Burial and preservation of carbonate rocks over Phanerozoic time. *Aquatic geochemistry*, **17** (4-5), 727–733.

Beversdorf, L.J., White, A.E., Björkman, K.M., Letelier, R.M. and Karl, D.M. 2010. Phosphonate metabolism by Trichodesmium IMS101 and the production of greenhouse gases. *Limnology and oceanography*, **55** (4), 1768–1778.

Bickert, T., Pätzold, J., Samtleben, C. and Munnecke, A. 1997. Paleoenvironmental changes in the Silurian indicated by stable isotopes in brachiopod shells from Gotland, Sweden. *Geochimica et Cosmochimica Acta*, **61**(13), 2717–2730.

Birgel, D., Meister, P., Lundberg, R., Horath, T.D., Bontognali, T.R.R., Bahniuk, A.M., de, Rezende, C.E., Vasconcelos, C. and McKenzie, J.A. 2015. Methanogenesis produces strong ^{13}C enrichment in stromatolites of Lagoa Salgada, Brazil: a modern analogue for Paleo-/Neoproterozoic stromatolites? *Geobiology*, **13** (3), 245–266.

Black, M. 1933. The precipitation of calcium carbonate on the Great Bahama Bank. *Geological Magazine*, **70** (10), 455–466.

Bojanowski, M.J. 2014. Authigenic dolomites in the Eocene–Oligocene organic carbon-rich shales from the Polish Outer

Carpathians: Evidence of past gas production and possible gas hydrate formation in the Silesian basin. *Marine and petroleum geology*, **51**, 117–135.

Bosak, T., Souza-Egipsy, V., Corsetti, F.A. and Newman, D.K. 2004. Micrometer-scale porosity as a biosignature in carbonate crusts. *Geology*, **32** (9), 781–784.

Botz, R., Pokojski, H. D., Schmitt, M. and Thomm, M. 1996. Carbon isotope fractionation during bacterial methanogenesis by CO_2 reduction. *Organic Geochemistry*, **25** (3-4), 255–262.

Bowman, C.N., Young, S.A., Kaljo, D., Eriksson, M.E., Them, T.R., Hints, O., Martma, T. and Owens, J.D. 2019. Linking the progressive expansion of reducing conditions to a stepwise mass extinction event in the late Silurian oceans. *Geology*, **47** (10), 968–972.

Braissant, O., Cailleau, G., Dupraz, C. and Verrecchia, E.P. 2003. Bacterially induced mineralization of calcium carbonate in terrestrial environments: the role of exopolysaccharides and amino acids. *Journal of Sedimentary Research*, **73** (3), 485–490.

Brenchley, P.J., Marshall, J.D., Carden, G.A.F., Robertson, D.B.R., Long, D.G.F., Meidla, T., Hints, L. and Anderson, T.F. 1994. Bathymetric and isotopic evidence for a short-lived Late Ordovician glaciation in a greenhouse period. *Geology*, **22** (4), 295–298.

Broecker, W., Sanyal, A. and Takahashi, T. 2000. The origin of Bahamian whitings revisited. *Geophysical Research Letters*, **27** (22), 3759–3760.

Buczynski, C. and Chafetz, H.S. 1991. Habit of bacterially induced precipitates of calcium carbonate and the influence of medium vicosity on mineralogy. *Journal of Sedimentary Research*, **61** (2), 226–233.

Calner, M. 2008. Silurian global events – at the tipping point of climate change. In: Elewa, A.M.T. (Ed.), Mass extinction, 21–58. Springer-Verlag; Heidelberg.

Calvert, S.E., Karlin, R.E., Toolin, L.J., Donahue, D.J., Southon, J.R. and Vogel, J.S. 1991. Low organic carbon accumulation rates in Black Sea sediments. *Nature*, **350** (6320), 692.

Calvert, S.E. and Karlin, R.E. 1998. Organic carbon accumulation in the Holocene sapropel of the Black Sea. *Geology*, **26** (2), 107–110.

Capone, D.G., Subramaniam, A., Montoya, J.P., Voss, M., Humborg, C., Johansen, A.M., Siefert, R. and Carpenter, E.J. 1998. An extensive bloom of the N_2-fixing cyanobacterium *Trichodesmium erythraeum* in the central Arabian Sea. *Marine Ecology Progress Series*, **172**, 281–292.

Carini, P., White, A.E., Campbell, E.O. and Giovannoni, S.J. 2014. Methane production by phosphate-starved SAR11 chemoheterotrophic marine bacteria. *Nature communications*, **5** (1), 1–7.

Chafetz, H.S. 2013. Porosity in bacterially induced carbonates: Focus on micropores. *AAPG bulletin*, **97 (**11), 2103–2111.

Cherns, L. and Wheeley, J.R. 2009. Early Palaeozoic cooling events: peri-Gondwana and beyond. *Geological Society, London, Special Publications*, **325** (1), 257–278.

Claypool, G.E. and Kaplan, I.R. 1974. The origin and distribution of methane in marine sediments. In: Kaplan, I.R. (Ed.), Natural Gases in Marine Sediments, 99–139. Plenum Press; New York.

Cocks, L.R.M. and Torsvik, T.H. 2005. Baltica from the late Precambrian to mid-Palaeozoic times: the gain and loss of a terrane's identity. *Earth-Science Reviews*, **72** (1), 39–66.

Davis, R.A., Reas, C. and Robbins, L. 1995. Calcite mud in a Holocene back-barrier lagoon; Lake Reeve, Victoria, Australia. *Journal of Sedimentary Research*, **65** (1a), 178–184.

De Groot, K. and Duyvis, E. 1966. Crystal form of precipitated calcium carbonate as influenced by adsorbed magnesium ions. *Nature*, **212** (5058), 183–184.

Degens, E.T. and Stoffers, P. 1976. Stratified waters as a key to the past. *Nature*, **263** (5572), 22.

Dela Pierre, F., Clari, P., Natalicchio, M., Ferrando, S., Giustetto, R., Lozar, F., Lugli, S., Manzi, V., Roveri, M. and Violanti, D. 2014. Flocculent layers and bacterial mats in the mudstone interbeds of the Primary Lower Gypsum Unit (Tertiary Piedmont Basin, NW Italy): archives of palaeoenvironmental changes during the Messinian salinity crisis. *Marine Geology*, **355**, 71–87.

Dittrich, M., Kurz, P. and Wehrli, B. 2004. The role of autotrophic picocyanobacteria in calcite precipitation in an oligotrophic lake. *Geomicrobiology Journal*, **21** (1), 45–53.

Dittrich, M. and Obst, M. 2004. Are picoplankton responsible for calcite precipitation in lakes? *AMBIO: A Journal of the Human Environment*, **33** (8), 559–564.

Dix, G.R. 2001. Origin of Sr-rich magnesian calcite mud in a Holocene pond basin (Lee Stocking Island, Bahamas). *Journal of Sedimentary Research*, **71** (1), 167–175.

Duque-Botero, F. and Florentin, J.-M.M. 2008. Role of cyanobacteria in Corg-rich deposits: an example from the Indidura Formation (Cenomanian–Turonian), northeastern Mexico. *Cretaceous Research*, **29** (5-6), 957–964.

Eisma, D. 1986. Flocculation and de-flocculation of suspended matter in estuaries. *Netherlands Journal of Sea Research*, **20** (2-3), 183–199.

Eriksson, M.J. and Calner, M. 2008. A sequence stratigraphical model for the Late Ludfordian (Silurian) of Gotland, Sweden: implications for timing between changes in sea level, palaeoecology, and the global carbon cycle. *Facies*, **54** (2), 253–276.

Farkaš, J., Frýda, J. and Holmden, C. 2016. Calcium isotope constraints on the marine carbon cycle and $CaCO_3$ deposition during the late Silurian (Ludfordian) positive $\delta^{13}C$ excursion. *Earth and Planetary Science Letters*, **451**, 31–40.

Folk, R.L. 1974. The natural history of crystalline calcium carbonate; effect of magnesium content and salinity. *Journal of Sedimentary Research*, **44** (1), 40–53.

Freytet, P. and Verrecchia, E. 1993. Complex calcitic crystalli-

zations in nostoc parmelioides kütz (Freshwater cyanobacterium): Rhombs around trichomes inside nostoc colonies and epiphytic bacterial microstromatolites. *Geomicrobiology Journal*, **11** (2), 77–84.

Frýda, J. and Manda, Š. 2013. A long-lasting steady period of isotopically heavy carbon in the late Silurian ocean: evolution of the $\delta^{13}C$ record and its significance for an integrated $\delta^{13}C$, graptolite and conodont stratigraphy. *Bulletin of Geosciences*, **88** (2), 463–482.

Ghienne, J.F., Desrochers, A., Vandenbroucke, T.R., Achab, A., Asselin, E., Dabard, M.P., Claude Farley, C., Loi, A., Paris, F., Wickson, S. and Veizer, J. 2014. A Cenozoic-style scenario for the end-Ordovician glaciation. *Nature Communications*, **5**, 4485.

Giddings, J.A. and Wallace, M.W. 2009. Facies-dependent $\delta^{13}C$ variation from a Cryogenian platform margin, South Australia: Evidence for stratified Neoproterozoic oceans? *Palaeogeography, Palaeoclimatology, Palaeoecology*, **271** (3-4), 196–214.

Gill, B.C., Lyons, T.W., Young, S.A., Kump, L.R., Knoll, A.H. and Saltzman, M.R. 2011. Geochemical evidence for widespread euxinia in the Later Cambrian ocean. *Nature*, **469** (7328), 80–83.

Glenn, C., Rajan, S., McMurtry, G. and Benaman, J. 1995. Geochemistry, mineralogy, and stable isotopic results from Ala Wai estuarine sediments: Records of hypereutrophication and abiotic whitings. *Pacific Science*, **49** (4), 367–399.

Goyet, C., Bradshaw, A.L. and Brewer, P.G. 1991. The carbonate system in the Black Sea. *Deep Sea Research Part A. Oceanographic Research Papers*, **38** (Supplement 2), 1049–1068.

Greenfield, L.J. 1963. Metabolism and concentration of calcium and magnesium and precipitation of calcium carbonate by a marine bacterium. *Annals of the New York Academy of Sciences*, **109** (1), 23–45.

Grimm, K.A., Lange, C.B. and Gill, A.S. 1997. Self-sedimentation of phytoplankton blooms in the geologic record. *Sedimentary Geology*, **110**, 151–161.

Heldal, M., Norland, S., Erichsen, E.S., Thingstad, T.F. and Bratbak, G. 2012. An unaccounted fraction of marine biogenic $CaCO_3$ particles. *PloS one*, **7** (10), e47887, 1–6.

Holmden, C., Panchuk, K. and Finney, S. 2012. Tightly coupled records of Ca and C isotope changes during the Hirnantian glaciation event in an epeiric sea setting. *Geochimica et Cosmochimica Acta*, **98**, 94–106.

Huff, W.D., Bergström, S.M. and Kolata, D.R. 2000. Silurian K-bentonites of the Dnestr Basin, Podolia, Ukraine. *Journal of the Geological Society*, **157** (2), 493–504.

Irwin, H., Curtis, C. and Coleman, M. 1977. Isotopic evidence for source of diagenetic carbonates formed during burial of organic carbon-rich sediments. *Nature*, **269**, 209–213.

Jannasch, H.W. 1991. Microbial processes in the Black Sea water column and top sediment: and overview. In: Izdar, E. and Murray, J.W. (Eds), Black Sea Oceanography; NATO Advanced Studies Institute Series, C351, 271–281. Kluwer Academic; Dordrecht.

Jaworowski, K. 1971. Sedimentary structures of the Upper Silurian siltstones in the Polish Lowland. *Acta Geologica Polonica*, **21** (4), 519–572.

Jaworowski, K. 2000. Facies analysis of the Silurian shale-siltstone succession in Pomerania (northern Poland). *Geological Quarterly*, **44** (3), 297–315.

Jeppsson, L. and Aldridge, R.J. 2000. Ludlow (late Silurian) oceanic episodes and events. *Journal of the Geological Society*, **157** (6), 1137–1148.

Jeppsson, L., Talent, J.A., Mawson, R., Andrew, A., Corradini, C., Simpson, A.J., Wigforss-Lange, J. and Schönlaub, H.P. 2012. Late Ludfordian correlations and the Lau event. In: Talent, J.A. (Ed.), Earth and Life, International Year of Planet Earth, 653–675. Springer Verlag; Heidelberg.

Jeppsson, L., Talent, J.A., Mawson, R., Simpson, A.J., Andrew, A.S., Calner, M., Whitford, D., Trotter, J.A., Sandström, O. and Caldon, H.J. 2007. High-resolution Late Silurian correlations between Gotland, Sweden, and the Broken River region, NE Australia: lithologies, conodonts and isotopes. *Palaeogeography, Palaeoclimatology, Palaeoecology*, **245** (1), 115–137.

Kaljo, D., Boucot, A.J., Corfield, R.M., Le Herisse, A., Koren, T.N., Kriz, J., Mannik, P., Marss, T., Nestor, V., Shaver, R.H., Siveter, D.J. and Viira, V. 1996. Silurian bio-events. In: Walliser, O.H. (Ed.), Global events and event stratigraphy in the Phanerozoic, 173–224. Springer; Berlin, Heidelberg.

Kaljo, D., Einasto, R., Martma, T., Märss, T., Nestor, V. and Viira, V. 2015. A bio-chemostratigraphical test of the synchroneity of biozones in the upper Silurian of Estonia and Latvia with some implications for practical stratigraphy. *Estonian Journal of Earth Sciences*, **64** (4), 267–283.

Kaljo, D., Grytsenko, V., Martma, T. and Mõtus, M.-A. 2007. Three global carbon isotope shifts in the Silurian of Podolia (Ukraine): stratigraphical implications. *Estonian Journal of Earth Sciences*, **56** (4), 205–220.

Kaljo, D., Kiipli, T. and Martma, T. 1997. Carbon isotope event markers through the Wenlock-Přídolí sequence at Ohesaare (Estonia) and Priekule (Latvia). *Palaeogeography, Palaeoclimatology, Palaeoecology*, **132** (1), 211–223.

Kaljo, D., Martma, T., Männik, P. and Viira, V. 2003. Implications of Gondwana glaciations in the Baltic late Ordovician and Silurian and a carbon isotopic test of environmental cyclicity. *Bulletin de la Société géologique de France*, **174** (1), 59–66.

Kaltenböck, E. and Herndl, G.J. 1992. Ecology of amorphous aggregations (marine snow) in the Northern Adriatic Sea. IV. Dissolved nutrients and the autotrophic community associated with marine snow. *Marine Ecology-Progress Series*, **87**, 147–147.

Karl, D.M., Beversdorf, L., Björkman, K.M., Church, M.J., Martinez, A. and Delong, E.F. 2008. Aerobic production of methane in the sea. *Nature Geoscience*, **1** (7), 473–478.

Kelts, K. and McKenzie, J. 1982. Diagenetic dolomite formation in Quaternary anoxic diatomiceous muds of Deep Sea Drilling Project Leg 64, Gulf of California. *Initial Reports of the Deep Sea Drilling Program*, **64**, 553–570.

Kempe, S. 1990. Alkalinity: the link between anaerobic basins and shallow water carbonates? *Naturwissenschaften*, **77** (9), 426–427.

Kempe, S. and Kaźmierczak, J. 1994. The role of alkalinity in the evolution of ocean chemistry, organization of living systems, and biocalcification processes. *Bulletin de l'Institut océanographique (Monaco)*, **13**, 61–117.

Kendall, C.G. and Alsharhan, A.S. 2011. Coastal Holocene carbonates of Abu Dhabi, UAE: depositional setting, geomorphology, and role of cyanobacteria in micritization. In: Kendall, C.G. St.C., Alsharhan, A.S., Jarvis, I. and Stevens, T. (Eds), Quaternary carbonate and evaporite sedimentary facies and their ancient analogues. *International Association of Sedimentologists Special Publication*, **43**, 205–220.

Koren, T. 1993. Main event levels in the evolution of the Ludlow graptolites. *Geological Correlation*, **1**, 44–52.

Koutsodendris, A., Brauer, A., Zacharias, I., Putyrskaya, V., Klemt, E., Sangiorgi, F. and Pross, J. 2015. Ecosystem response to human and climate-induced environmental stress on an anoxic coastal lagoon (Etoliko, Greece) since 1930 AD. *Journal of Paleolimnology*, **53** (3), 255–270.

Kozłowski, W. 2003. Age, sedimentary environment and palaeogeographical position of the Late Silurian oolitic beds in the Holy Cross Mountains (Central Poland). *Acta Geologica Polonica*, **53** (4), 341–357.

Kozłowski, W. 2015. Eolian dust influx and massive whitings during the kozlowski/Lau Event: carbonate hypersaturation as a possible driver of the mid-Ludfordian Carbon Isotope Excursion. *Bulletin of Geosciences*, **90**, 807–840.

Kozłowski, W., Domańska-Siuda, J. and Nawrocki, J. 2014. Geochemistry and petrology of the upper Silurian greywackes from the Holy Cross Mountains (Central Poland): implications for the Caledonian history of the southern part of the Trans-European Suture Zone (TESZ). *Geological Quarterly*, **58** (1), 311–336.

Kozłowski, W. and Munnecke, A. 2010. Stable carbon isotope development and sea-level changes during the Late Ludlow (Silurian) of the Łysogóry region (Rzepin section, Holy Cross Mountains, Poland). *Facies*, **56** (4), 615–633.

Kozłowski, W. and Sobień, K. 2012. Mid-Ludfordian coeval carbon isotope, natural gamma ray and magnetic susceptibility excursions in the Mielnik IG-1 borehole (Eastern Poland)—dustiness as a possible link between global climate and the Silurian carbon isotope record. *Palaeogeography, Palaeoclimatology, Palaeoecology*, **339**, 74–97.

Kranz, S.A., Gladrow, D.W., Nehrke, G., Langer, G. and Rosta, B. 2010. Calcium carbonate precipitation induced by the growth of the marine cyanobacteria Trichodesmium. *Limnology and Oceanography*, **55** (6), 2563–2569.

Kump, L.R. and Arthur, M.A. 1999. Interpreting carbon-isotope excursions: carbonates and organic matter. *Chemical Geology*, **161** (1), 181–198.

Kump, L.R., Arthur, M.A., Patzkowsky, M.E., Gibbs, M.T., Pinkus, D.S. and Sheehan, P.M. 1999. A weathering hypothesis for glaciation at high atmospheric pCO_2 during the Late Ordovician. *Palaeogeography, Palaeoclimatology, Palaeoecology* **152**, 173–187.

Lalou, C. 1957. Studies on bacterial precipitation of carbonates in sea water. *Journal of Sedimentary Research*, **27** (2), 190–195.

Lampitt, R., Wishner, K., Turley, C. and Angel, M. 1993. Marine snow studies in the Northeast Atlantic Ocean: distribution, composition and role as a food source for migrating plankton. *Marine Biology*, **116** (4), 689–702.

LaPorte, D.F., Holmden, C., Patterson, W.P., Loxton, J.D., Melchin, M.J., Mitchell, C.E., Finney, S.C. and Sheets, H.D. 2009. Local and global perspectives on carbon and nitrogen cycling during the Hirnantian glaciation. *Palaeogeography, Palaeoclimatology, Palaeoecology*, **276** (1-4), 182–195.

Lee, J. and Morse, J.W. 2010. Influences of alkalinity and p CO_2 on $CaCO_3$ nucleation from estimated Cretaceous composition seawater representative of "calcite seas". *Geology*, **38** (2), 115–118.

Lehnert, O., Frýda, J., Buggisch, W., Munnecke, A., Nützel, A., Kříž, J. and Manda, S. 2007. $\delta^{13}C$ records across the late Silurian Lau event: New data from middle palaeo-latitudes of northern peri-Gondwana (Prague Basin, Czech Republic). *Palaeogeography, Palaeoclimatology, Palaeoecology,* **245** (1), 227–244.

Long, J.S., Hu, C., Robbins, L.L., Byrne, R.H., Paul, J.H. and Wolny, J.L. 2017. Optical and biochemical properties of a southwest Florida whiting event. *Estuarine, Coastal and Shelf Science*, **196**, 258–268.

Lowenstein, T.K., Hardie, L.A., Timofeeff, M.N. and Demicco, R.V. 2003. Secular variation in seawater chemistry and the origin of calcium chloride basinal brines. *Geology*, **31** (10), 857–860.

Lowenstein, T.K., Timofeeff, M.N., Brennan, S.T., Hardie, L.A. and Demicco, R.V. 2001. Oscillations in Phanerozoic seawater chemistry: Evidence from fluid inclusions. *Science*, **294** (5544), 1086–1088.

Loydell, D.K. 2007. Early Silurian positive $\delta^{13}C$ excursions and their relationship to glaciations, sea-level changes and extinction events. *Geological Journal*, **42** (5), 531–546.

Loydell, D.K. and Frýda, J. 2011. At what stratigraphical level is the mid Ludfordian (Ludlow, Silurian) positive carbon isotope excursion in the type Ludlow area, Shropshire, England. *Bulletin of Geosciences*, **86** (2), 197–208.

Macquaker, J.H., Keller, M.A. and Davies, S.J. 2010. Algal blooms and "marine snow": Mechanisms that enhance preservation of organic carbon in ancient fine-grained sediments. *Journal of Sedimentary Research*, **80** (11), 934–942.

Major, C., Ryan, W., Lericolais, G. and Hajdas, I. 2002. Constraints on Black Sea outflow to the Sea of Marmara during

the last glacial-interglacial transition. *Marine Geology*, **190** (1), 19–34.

Manville, V. and Wilson, C. 2004. Vertical density currents: a review of their potential role in the deposition and interpretation of deep-sea ash layers. *Journal of the Geological Society*, **161** (6), 947–958.

Martma, T., Brazauskas, A., Kaljo, D., Kaminskas, D. and Musteikis, P. 2010. The Wenlock–Ludlow carbon isotope trend in the Vidukle core, Lithuania, and its relations with oceanic events. *Geological Quarterly*, **49** (2), 223–234.

Meister, P., Gutjahr, M., Frank, M., Bernasconi, S.M., Vasconcelos, C. and McKenzie, J.A. 2011. Dolomite formation within the methanogenic zone induced by tectonically driven fluids in the Peru accretionary prism. *Geology*, **39**, 563–566.

Meister, P., Liu, B., Khalili, A., Böttcher, M.E. and Jørgensen, B.B. 2019. Factors controlling the carbon isotope composition of dissolved inorganic carbon and methane in marine porewater: An evaluation by reaction-transport modelling. *Journal of Marine Systems*, **200**, 103227.

Melchin, M.J. and Holmden, C. 2006a. Carbon isotope chemostratigraphy of the Llandovery in Arctic Canada: implications for global correlation and sea-level change. *GFF*, **128** (2), 173–180.

Melchin M.J. and Holmden C. 2006b. Carbon isotope chemostratigraphy in Arctic Canada: sea-level forcing of carbonate platform weathering and implications for Hirnantian global correlation. *Palaeogeography, Palaeoclimatology, Palaeoecology* **234**, 186–200.

Middelburg, J.J., Vlug, T., Jaco, F. and Van der Nat, W. A. 1993. Organic matter mineralization in marine systems. *Global and Planetary Change*, **8** (1-2), 47–58.

Minoletti, F., De Rafélis, M., Renard, M., Gardin, S. and Young, J. 2005. Changes in the pelagic fine fraction carbonate sedimentation during the Cretaceous–Paleocene transition: contribution of the separation technique to the study of Bidart section. *Palaeogeography, Palaeoclimatology, Palaeoecology*, **216** (1-2), 119–137.

Modliński, Z., Szymański, B. and Teller, L. 2006. Litostratygrafia syluru polskiej części obniżenia perybałtyckiego – część lądowa i morska (N Polska). *Przegląd Geologiczny*, **54** (9), 787–796.

Morita, R.Y. 1980. Calcite precipitation by marine bacteria. *Geomicrobiology Journal*, **2** (1), 63–82.

Morse, J.W., Gledhill, D.K. and Millero, F.J. 2003. $CaCO_3$ precipitation kinetics in waters from the great Bahama bank:: Implications for the relationship between bank hydrochemistry and whitings. *Geochimica et Cosmochimica Acta*, **67** (15), 2819–2826.

Morse, J.W. and He, S. 1993. Influences of T, S and pCO_2 on the pseudo-homogeneous precipitation of $CaCO_3$ from seawater: implications for whiting formation. *Marine Chemistry*, **41** (4), 291–297.

Morse, J.W., Millero, F.J., Thurmond, V., Brown, E. and Ostlund, H. 1984. The carbonate chemistry of Grand Bahama Bank waters: after 18 years another look. *Journal of Geophysical Research: Oceans*, **89** (C3), 3604–3614.

Mucci, A. and Morse, J.W. 1983. The incorporation of Mg^{2+} and Sr^{2+} into calcite overgrowths: influences of growth rate and solution composition. *Geochimica et Cosmochimica Acta*, **47** (2), 217–233.

Müller, A. 2001. Geochemical expressions of anoxic conditions in Nordåsvannet, a land-locked fjord in western Norway. *Applied Geochemistry*, **16** (3), 363–374.

Müller, G. and Blaschke, R. 1969. Zur Entstehung des Tiefsee-Kalkschlammes im Schwarzen Meer. *Naturwissenschaften*, **56** (11), 561–562.

Munnecke, A., Calner, M., Harper, D.A. and Servais, T. 2010. Ordovician and Silurian sea-water chemistry, sea level, and climate: A synopsis. *Palaeogeography, Palaeoclimatology, Palaeoecology*, **296** (3), 389–413.

Munnecke, A., Samtleben, C. and Bickert, T. 2003. The Ireviken Event in the lower Silurian of Gotland, Sweden–relation to similar Palaeozoic and Proterozoic events. *Palaeogeography, Palaeoclimatology, Palaeoecology*, **195** (1), 99–124.

Nezlin, N.P., Polikarpov, I.G., Al-Yamani, F.Y., Rao, D.S. and Ignatov, A.M. 2010. Satellite monitoring of climatic factors regulating phytoplankton variability in the Arabian (Persian) Gulf. *Journal of Marine Systems*, **82** (1-2), 47–60.

Nielsen, M.R., Sand, K.K., Rodriguez-Blanco, J.D., Bovet, N., Generosi, J., Dalby, K.N. and Stipp, S.L.S. 2016. Inhibition of Calcite Growth: Combined Effects of Mg^{2+} and SO_4^{2-}. *Crystal Growth & Design*, **16** (11), 6199–6207.

Noble, P.J., Lenz, A.C., Holmden, C., Masiak, M., Zimmerman, M.K., Poulson, S.R. and Kozłowska, A. 2012. Isotope geochemistry and plankton response to the Ireviken (earliest Wenlock) and *Cyrtograptus lundgreni* extinction events, Cape Phillips Formation, Arctic Canada. In: Talent, J.A. (Ed.), Earth and Life, 631–652, Springer; Dordrecht.

Peryt, T.M., Durakiewicz, T., Kotarba, M.J., Oszczepalski, S. and Peryt, D. 2012. Carbon isotope stratigraphy of the basal Zechstein (Lopingian) strata in Northern Poland and its global correlation. *Geological Quarterly*, **56** (2), 285–298.

Pierre, C., Ortlieb, L. and Person, A. 1984. Supratidal evaporitic dolomite at Ojo de Liebre Lagoon; mineralogical and isotopic arguments for primary crystallization. *Journal of Sedimentary Research*, **54** (4), 1049–1061.

Pilskaln, C.H. and Pike, J. 2001. Formation of Holocene sedimentary laminae in the Black Sea and the role of the benthic flocculent layer. *Paleoceanography*, **16** (1), 1–19.

Poprawa, P., Šliaupa, S., Stephenson, R. and Lazauskiene, J. 1999. Late Vendian–Early Palaeozoic tectonic evolution of the Baltic Basin: regional tectonic implications from subsidence analysis. *Tectonophysics*, **314** (1), 219–239.

Porębska, E., Kozłowska-Dawidziuk, A. and Masiak, M. 2004. The lundgreni event in the Silurian of the East European Platform, Poland. *Palaeogeography, Palaeoclimatology, Palaeoecology*, **213** (3-4), 271–294.

Porębski, S.J. and Podhalańska, T. 2019. Ordovician–Silurian

lithostratigraphy of the East European Craton in Poland, *Annales Societatis Geologorum Poloniae*, **87** (5), 95–104.

Porębski, S.J., Prugar, W. and Zacharski, J. 2013. Silurian shales of the East European Platform in Poland – some exploration problems. *Przegląd Geologiczny*, **61** (11), 630–638.

Ransom, B., Shea, K.F., Burkett, P.-J., Bennett, R.H., and Baerwald, R. 1998. Comparison of pelagic and nepheloid layer marine snow: implications for carbon cycling. *Marine Geology*, **150**, 39–50.

Reichel, T. and Halbach, P. 2007. An authigenic calcite layer in the sediments of the Sea of Marmara – A geochemical marker horizon with paleoceanographic significance. *Deep Sea Research Part II: Topical Studies in Oceanography*, **54** (11), 1201–1215.

Ridgwell, A. 2005. A Mid Mesozoic Revolution in the regulation of ocean chemistry. *Marine Geology*, **217** (3), 339–357.

Ridgwell, A. and Zeebe, R.E. 2005. The role of the global carbonate cycle in the regulation and evolution of the Earth system. *Earth and Planetary Science Letters*, **234** (3), 299–315.

Riding, R. 1982. Cyanophyte calcification and changes in ocean chemistry. *Nature*, **299** (5886), 814–815.

Riebesell, U. 1991. Particle aggregation during a diatom bloom I. Physical aspects. *Marine Ecology Progress Series*, **69**, 273–280.

Robbins, L. and Blackwelder, P. 1992. Biochemical and ultrastructural evidence for the origin of whitings: a biologically induced calcium carbonate precipitation mechanism. *Geology*, **20** (5), 464–468.

Robbins, L., Tao, Y. and Evans, C. 1997. Temporal and spatial distribution of whitings on Great Bahama Bank and a new lime mud budget. *Geology*, **25** (10), 947–950.

Rosenbaum, J. and Sheppard, S.M. 1986. An isotopic study of siderites, dolomites and ankerites at high temperatures. *Geochimica et Cosmochimica Acta*, **50** (6), 1147–1150.

Rubin, M., Berman-Frank, I. and Shaked, Y. 2011. Dust-and mineral-iron utilization by the marine dinitrogen-fixer Trichodesmium. *Nature Geoscience*, **4** (8), 529–534.

Saitoh, M., Ueno, Y., Isozaki, Y., Shibuya, T., Yao, J., Ji, Z., Shozugawa, K., Matuso, M.and Yoshida, N. 2015. Authigenic carbonate precipitation at the end-Guadalupian (Middle Permian) in China: implications for the carbon cycle in ancient anoxic oceans. *Progress in Earth and Planetary Science*, **2** (1), 41–60.

Samtleben, C., Munnecke, A. and Bickert, T. 2000. Development of facies and C/O-isotopes in transects through the Ludlow of Gotland: evidence for global and local influences on a shallow-marine environment. *Facies*, **43** (1), 1–38.

Sánchez-Baracaldo, P. 2015. Origin of marine planktonic cyanobacteria. *Scientific Reports*, **5**, 17418.

Schimmelmann, A., Lange, C. B., Schieber, J., Francus, P., Ojala, A. E. and Zolitschka, B. 2016. Varves in marine sediments: a review. *Earth-Science Reviews*, **159**, 215–246.

Shinn, E.A., Steinen, R.P., Lidz, B.H. and Swart, P.K. 1989. Whitings, a Sedimentologic Dilemma. *Journal of Sedimentary Research*, **59** (1), 147–161.

Sondi, I. and Juračić, M. 2010. Whiting events and the formation of aragonite in Mediterranean Karstic Marine Lakes: new evidence on its biologically induced inorganic origin. *Sedimentology*, **57** (1), 85–95.

Spiridonov, A., Stankevič, R., Gečas, T., Šilinskas, T., Brazauskas, A., Meidla, T., Ainsaar, L., Musteiklis, P. and Radzevičius, S. 2017. Integrated record of Ludlow (Upper Silurian) oceanic geobioevents – Coordination of changes in conodont, and brachiopod faunas, and stable isotopes. *Gondwana Research*, **51**, 272–288.

Stachowitsch, M., Fanuko, N. and Richter, M. 1990. Mucus aggregates in the Adriatic Sea: an overview of stages and occurrences. *Marine Ecology*, **11** (4), 327–350.

Stoffers, P. and Müller, G. 1978. Mineralogy and lithofacies of Black Sea sediments, Leg 42B deep sea drilling project. *Initial Reports of the Deep Sea Drilling Project*, **42** (2), 373–411.

Sweeney, M., Turner, P. and Vaughan, D. 1987. The Marl Slate: a model for the precipitation of calcite, dolomite and sulfides in a newly formed anoxic sea. *Sedimentology*, **34** (1), 31–48.

Taylor, M., Drysdale, R. and Carthew, K. 2004. The formation and environmental significance of calcite rafts in tropical tufa-depositing rivers of northern Australia. *Sedimentology*, **51** (5), 1089–1101.

Teller, L. 1966. Two new species of Monograptidae from the Upper Ludlovian of Poland. *Bulletin de l'Academie Polonaise des Sciences*, II, **14**, 553–558.

Thompson, J.B. 2000. Microbial whitings, In: Riding, R.E. and Awramik, S.M. (Eds), Microbial sediments, 250–260. Springer; Berlin, Heidelberg.

Thompson, J.B., Schultze-Lam, S., Beveridge, T.J. and Des Marais, D.J. 1997. Whiting events: biogenic origin due to the photosynthetic activity of cyanobacterial picoplankton. *Limnology and oceanography*, **42** (1), 133–141.

Tomczyk, H. 1970. The Silurian. In: Sokołowski, S. (Ed.), The Geology of Poland, 237–320. Wydawnictwa Geologiczne; Warsaw.

Tomczyk, H. 1973. Silurian. In: Szyperko-Teller, A. (Ed.), Profile głębokich otworów wiertniczych Instytutu Geologicznego: Pasłęk IG-1, 57–95. Wydawnictwa Geologiczne; Warszawa.

Topulos, T. 1976. Results of geophisical study – Lower Palaeozoic and Precambrian. In: Witkowski, A. (Ed.), Profile głębokich otworów wiertniczych Instytutu Geologicznego: Żarnowiec IG 1, 156–163. Wydawnictwa Geologiczne; Warszawa. [In Polish]

Topulos, T. 1977. Characteristic of the Silurian in the Peribaltic Syneclise based on geophysical reaserch. *Geological Quarterly*, **21** (3), 437–450. [In Polish]

Tourney, J. and Ngwenya, B.T. 2009. Bacterial extracellular polymeric substances (EPS) mediate $CaCO_3$ morphology and polymorphism. *Chemical Geology*, **262** (3), 138–146.

Tribble, J.S. and Mackenzie, F.T. 1998. Recrystallization of Magnesian Calcite Overgrowths on Calcite Seeds Suspended in Seawater. *Aquatic Geochemistry*, **4** (3), 337–360.

Troy, P.J., Li, Y.-H. and Mackenzie, F.T. 1997. Changes in Surface Morphology of Calcite Exposed to the Oceanic Water Column. *Aquatic Geochemistry*, **3** (1), 1–20.

Tsegelnjuk, P.D. 1976. Late Silurian and Early Devonian monograptids from the South-Western margin of the East European Platform. In: Shulga, P.L. (Ed.), Palaeontology and stratigraphy of the Upper Precambrian and Lower Paleozoic of the SW part of the East European Platform, 9, 1–133. Naukova Dumka; Kiev. [In Russian]

Underwood, C.J., Crowley, S., Marshall, J. and Brenchley, P. 1997. High-resolution carbon isotope stratigraphy of the basal Silurian Stratotype (Dob's Linn, Scotland) and its global correlation. *Journal of the Geological Society*, **154** (4), 709–718.

Urbanek, A. 1993. Biotic crises in the history of Upper Silurian graptoloids: a palaeobiological model. *Historical Biology*, **7** (1), 29–50.

Urbanek, A. 1997. Late Ludfordian and early Přídolí monograptids from the Polish Lowland. *Acta Palaeontologica Polonica*, **56**, 87–231.

van der Jagt, H., Friese, C., Stuut, J.B.W., Fischer, G. and Iversen, M.H. 2018. The ballasting effect of Saharan dust deposition on aggregate dynamics and carbon export: Aggregation, settling, and scavenging potential of marine snow. *Limnology and Oceanography*, **63** (3), 1386–1394.

Vasconcelos, C., McKenzie, J.A., Warthmann, R. and Bernasconi, S.M. 2005. Calibration of the $\delta^{18}O$ paleothermometer for dolomite precipitated in microbial cultures and natural environments. *Geology*, **33** (4), 317–320.

Wallmann, K., Aloisi, G., Haeckel, M., Tishchenko, P., Pavlova, G., Greinert, J., Kutterolf, S. and Eisenhauer, A. 2008. Silicate weathering in anoxic marine sediments. *Geochim. Cosmochim. Acta* **72**, 3067–3090.

Wells, A. and Illing, L. 1964. Present-day precipitation of calcium carbonate in the Persian Gulf. *Developments in sedimentology*, **1**, 429–435.

Wenzel, B. and Joachimski, M.M. 1996. Carbon and oxygen isotopic composition of Silurian brachiopods (Gotland/Sweden): palaeoceanographic implications. *Palaeogeography, Palaeoclimatology, Palaeoecology*, **122** (1-4), 143–166.

Wignall, P., and Newton, R. 1998. Pyrite framboid diameter as a measure of oxygen deficiency in ancient mudrocks. *American Journal of Science*, **298** (7), 537–552.

Wilkin, R. and Barnes, H. 1997. Formation processes of framboidal pyrite. *Geochimica et Cosmochimica Acta*, **61** (2), 323–339.

Wilkin, R.T., Barnes, H.L. and Brantley, S.L. 1996. The size distribution of framboidal pyrite in modern sediments: An indicator of redox conditions. *Geochimica et Cosmochimica Acta*, **60**, 3897–3912.

Wilson, P.A. and Roberts, H.H. 1992. Carbonate-periplatform sedimentation by density flows: a mechanism for rapid off-bank and vertical transport of shallow-water fines. *Geology*, **20** (8), 713–716.

Wollast, R., Garrels, R. and Mackenzie, F. 1980. Calcite-seawater reactions in ocean surface waters. *American Journal of Science*, **280** (9), 831–848.

Wright, D.T. and Oren, A. 2005. Nonphotosynthetic bacteria and the formation of carbonates and evaporites through time. *Geomicrobiology Journal*, **22** (1-2), 27–53.

Wu, Y.S., Yu, G.L., Li, R.H., Song, L.R., Jiang, H.X., Riding, R., Liu, L.-J., Liu, D.-J. and Zhao, R. 2014. Cyanobacterial fossils from 252 Ma old microbialites and their environmental significance. *Scientific reports*, **4** (1), 1–5.

Wu, Y.-S., Yu, G.-L., Jiang, H.-X., Liu, L.-J. and Zhao, R. 2016. Role and lifestyle of calcified cyanobacteria (Stanieria) in Permian–Triassic boundary microbialites. *Palaeogeography, Palaeoclimatology, Palaeoecology*, **448**, 39–47.

Yao, W. and Millero, F.J. 1995. The chemistry of the anoxic waters in the Framvaren Fjord, Norway. *Aquatic Geochemistry*, **1** (1), 53–88.

Yates, K. and Robbins, L. 2001. Microbial lime-mud production and its relation to climate change. In: Gerhard, L.C., Harrison, W.E. and Hanson, B.M. (Eds), Geological Perspectives of Global Climate Change. *AAPG Studies in Geology*, **47**, 267–283.

Yates, K.K. and Robbins, L.L. 1998. Production of carbonate sediments by a unicellular green alga. *American Mineralogist*, **83** (11), 1503–1509.

Younes, H., Calner, M. and Lehnert, O. 2017. The first continuous $\delta^{13}C$ record across the Late Silurian Lau Event on Gotland, Sweden. *GFF*, **139** (1), 63–69.

Zeebe, R.E. and Westbroek, P. 2003. A simple model for the $CaCO_3$ saturation state of the ocean: The "Strangelove," the "Neritan," and the "Cretan" Ocean. *Geochemistry, Geophysics, Geosystems*, **4** (12), 1–26.

Zenkner, L.J. and Kozłowski, W. 2017. Anomalous massive water-column carbonate precipitation (whitings) as another factor linking Silurian oceanic events. *GFF*, **139** (3), 184–194.

Manuscript submitted: 16st January 2020
Revised version accepted: 2nd July 2020